

ENGINEERING AND CHARACTERIZATION OF SINGLE PHOTON EMITTING
DEFECTS IN HEXAGONAL BORON NITRIDE

by

JOSHUA ZIEGLER

A DISSERTATION

Presented to the Department of Physics
and the Graduate School of the University of Oregon
in partial fulfillment of the requirements
for the degree of
Doctor of Philosophy

June 2020

DISSERTATION APPROVAL PAGE

Student: Joshua Ziegler

Title: Engineering and Characterization of Single Photon Emitting Defects in Hexagonal Boron Nitride

This dissertation has been accepted and approved in partial fulfillment of the requirements for the Doctor of Philosophy degree in the Department of Physics by:

Hailin Wang	Chairperson
Benjamín Alemán	Advisor
Dietrich Belitz	Core Member
Mark Lonergan	Institutional Representative

and

Kate Mondloch	Vice Provost and Dean of the Graduate School
---------------	--

Original approval signatures are on file with the University of Oregon Graduate School.

Degree awarded 2020

© 2020 Joshua Ziegler

DISSERTATION ABSTRACT

Joshua Ziegler

Doctor of Philosophy

Department of Physics

June 2020

Title: Engineering and Characterization of Single Photon Emitting Defects in Hexagonal Boron Nitride

Single photons have broad applications across quantum information technologies including quantum computation, boson sampling, and quantum communication. Current single photon generation techniques are not ideal due to concerns such as low brightness, stochasticity, or need for low temperatures. The recently discovered single photon emitter in the 2D material hexagonal boron nitride is an interesting single photon source due to its extreme brightness and photoluminescence stability. Moreover, the nanoscale thickness of the material allows for strong coupling to hybrid photonic structures. However, integration of these single photon emitters has not yet been reliably realized due to a large amount of inhomogeneous broadening (which may be due to strain) and difficulties in consistent fabrication of these emitters. If these two problems could be solved, the viability of integrating these emitters would be greatly increased.

Here, we address wavelength variation in boron nitride emitters by identifying a zero-dimensional boron nitride nanostructure that hosts single photon emitters with reduced spectral variation. We find that these emitters in this nanostructure have a wavelength variation reduced by a factor of 5. We offer reasoning that this may be due to the mechanical robustness of the zero-dimensional structure.

In order to reliably fabricate these emitters, we develop a focused ion beam milling technique to create single photon emitters by cutting holes in the hexagonal boron nitride. Optimally tuning the milling parameters, we achieve a 31% yield of sites with the signature of single photon emission and a 94% yield of sites that have the signature of few photon emission.

Together, these two results open the door for large-scale on-chip integration of boron nitride emitters into photonic or plasmonic structures. More engineering is likely needed for further control of emission wavelength as well as reduction of the two-photon probability, but our results will be invaluable for practical uses of hexagonal boron nitride single photon emitters.

This dissertation includes previously published coauthored material.

CURRICULUM VITAE

NAME OF AUTHOR: Joshua Ziegler

GRADUATE AND UNDERGRADUATE SCHOOLS ATTENDED:

University of Oregon, Eugene, OR
California Polytechnic State University, San Luis Obispo, CA

DEGREES AWARDED:

Doctor of Philosophy, 2020, University of Oregon
Bachelor of Science, Physics, 2015, California Polytechnic State University

AREAS OF SPECIAL INTEREST:

Quantum information technology
Color centers in large bandgap semiconductors
2D Materials
Materials characterization

PROFESSIONAL EXPERIENCE:

Graduate Research Assistant, Alemán Lab, University of Oregon, Eugene,
Oregon, 2016-2020

Graduate Teaching Assistant, Department of Physics, University of Oregon,
Eugene, Oregon, 2015-2020

GRANTS, AWARDS, AND HONORS:

Ovshinsky Travel Grant Award, APS: Division of Materials Physics, 2019

J.W. Van Dyke Scholarship, California Polytechnic State University, 2014

Generation 1st Degree Scholarship, Hispanic Scholarship Fund, 2012

PUBLICATIONS:

- (1) Ziegler, J.; Blaikie, A.; Fathalizadeh, A.; Miller, D.; Yasin, F. S.; Williams, K.; Mohrhardt, J.; McMorran, B. J.; Zettl, A.; Alemán, B. Single-Photon Emitters in Boron Nitride Nanococoons. *Nano Lett.* **2018**, *18* (4), 2683–2688.

- (2) Ziegler, J.; Klaiss, R.; Blaikie, A.; Miller, D.; Horowitz, V. R.; Alemán, B. J. Deterministic Quantum Emitter Formation in Hexagonal Boron Nitride via Controlled Edge Creation. *Nano Lett.* 2019, 19 (3), 2121–2127.
- (3) Ziegler, J.; Echols, S.; Moelter, M. J.; Saunders, K. Type-I and Type-II Smectic-C* Systems: A Twist on the Electroclinic Critical Point. *Phys. Rev. E* 2019, 100 (2), 022707.

ACKNOWLEDGMENTS

The work described in this dissertation would not have been possible without the guidance and support of my advisor Prof. Benjamín Alemán. Not only has he been an endless font of insight for research and writing, he has been instrumental for my development as an independent and capable scientist and science communicator. I would also like to thank the members of the Alemán lab who have all been indispensable sources of expertise and company, including Rudy Resch, Andrew Blaikie, David Miller, Kara Zappitelli, Rachael Klaiiss, and Brittany Carter. This sentiment is shared towards my collaborator, Prof. Viva Horowitz. I also would like to thank my thesis committee for their support and insights.

And of course, I wouldn't be here if it weren't for the unconditional support given to me from my family, my girlfriend Nicole, and my beautiful baby dog Ruby.

TABLE OF CONTENTS

Chapter	Page
I. INTRODUCTION.....	1
1.1. Why single photons?.....	1
1.2. Why hexagonal boron nitride?.....	2
1.3. Limitations and how we tried to beat them.....	3
II. MEASURING SINGLE PHOTON EMISSION: THE SECOND ORDER CORRELATION FUNCTION	5
2.1. Introduction.....	5
2.2. Mathematical modeling	6
2.3. Possible issues.....	8
2.3. Bridge.....	9
III. SINGLE PHOTON EMITTERS IN BORON NITRIDE NANOCOCOONS	10
3.1. Introduction.....	10
3.2. Materials and methods	12
3.3. Results and discussion	16
3.4. Conclusion	22
3.5. Supplementary information	23
3.6. Bridge.....	27
IV. DETERMINISTIC QUANTUM EMITTER FORMATION IN HEXAGONAL BORON NITRIDE BY CONTROLLED EDGE CREATION.....	28

4.1. Introduction.....	28
4.2. Results and discussion	40
4.3. Conclusion	40
4.4. Materials and methods	40
4.5. Supplementary Information	41
V. CONCLUDING REMARKS.....	50
REFERENCES CITED.....	52

LIST OF FIGURES

Figure	Page
3.1. (a) High resolution transmission electron microscopy image of a BNNC on a BNNT showing its wall and hollow interior (b) A sketch of a BNNC cross section emphasizing the locally flat faces.....	11
3.2. (a) Confocal image of a BNNC that hosts a SPE with an arbitrary intensity scale. (b) Low magnification SEM image of the BNNC that hosted a SPE on lacey carbon. (c) High magnification SEM image of the same BNNC on lacey carbon (d) TEM image of the BNNC on lacey carbon (e) Sketch of our optical setup (f) $g^2(t)$ for a single BNNC showing that $g^2(0) = 0.25$ – proving it is a SPE.....	14
3.3 (a) Confocal image of aggregated BN nanomaterial on lacey carbon with an arbitrary intensity scale. (b) Low magnification TEM image of aggregated BN nanomaterial on lacey carbon. (c) High magnification TEM image of the material (d) $g^2(t)$ for a single BNNC showing that $g^2(0) = 0.44$	15
3.4. (a) Representative spectra for different SPEs with a range from 564-603 nm, normalized for clarity. The box and swarm plots summarize the ZPL data of spectra obtained. (b) PL intensity vs Power curve (c) Polarization vs. PL intensity	18
3.5. (a) Spectra for the bright and dim state showing a reduction in ZPL and overall PL intensity without a corresponding change in wavelength. (b) $g^2(t)$ for the bright state – the lifetime was 2.59 ns and $g^2(0) = 0.34$ (c) $g^2(t)$ for the dim state - the lifetime was 0.83 ns and $g^2(0) = 0.38$	20
3.6. (a)-(l) All spectra obtained from SPEs found in BNNCs on lacey carbon. All of these spectra were considered when calculating the average zero phonon line and phonon sideband (PSB) of the BNNCs	24
3.7. (a) Confocal image of a sample, with the SPE that exhibited photodynamics circled in white (b) SEM image of the same area of the sample. (c) Low magnification TEM image of the same area. (d) High magnification TEM image of the SPE showing the large amount of BNNCs present	25
3.8. (a) Confocal image of a sample, with a SPE circled in white (b) SEM image	

Figure	Page
of the same area of the sample. (c) Low magnification TEM image of the same area. (d) High magnification TEM image of the SPE showing the large amount of BNNCs present	26
3.9. (a) Confocal image of a sample, with a SPE circled in white (b) SEM image of the same area of the sample. (c) Low magnification TEM image of the same area. (d) High magnification TEM image of the SPE showing the large amount of BNNCs present	27
4.1. (a) AFM image of a FIB milled region of hBN, with a line cut shown below. (b) Example of $g^2(t)$ data for a single QE in Region 2 showing $g^2(0) = 0.33$, well below the antibunching threshold for a single QE. (left) 60 ns time window centered about $t = 0$. (right) 800 ns window of the same data.....	30
4.2. Confocal, AFM and representative photoluminescence spectra for QEs made with various FIB parameters	31
4.3. Distributions of degree of antibunching for both regions of FIB-treated CVD hBN (Region 2).....	33
4.4. Zero phonon line energies across all emitters for which there was a clearly identifiable central emission line showing a similar distribution of energies compared to previous observations of hBN quantum emitters	36
4.5. (a) PL intensity of the single QEs. The last one, labeled QE10, shows blinking behavior that we analyze in b and c. (b) Probability density of the dim state lifetime. (c) Probability density of the bright state lifetime	37
4.6. Distributions of degree of antibunching for both regions of FIB-treated CVD hBN (Region 2).....	42
4.7. (a) Confocal image of a region (milled at high energy, low dose) of CVD hBN showing very poor visibility of the array (b) AFM image of the same region showing the large amount of wrinkles	43
4.8. (a) Atomic force microscope image of a region of CVD hBN nearby the FIBed regions characterized. (b) Confocal microscope image of unmilled hBN. (c) Plot of photoluminescence intensity vs. excitation power. (d) Spectrum of a low wavelength emitter	44

Figure	Page
4.9. Photoluminescence trajectories. Left: Photoluminescence (PL) intensity versus time for QE1 to 10. Right: Histograms corresponding to each trajectory	45
4.10. The bright state and dim state of QE9 both show an increase in PL intensity as the excitation laser power is increased.	46
4.11. There is no clear trend between each bright state duration and the previous bright state duration (blue) nor between each dim state duration and the previous dim state duration (green)	46
4.12. Probability density of duration of each state for QE9. The dim state (a) shows a dominant power law with slope $\alpha=1.75 \pm 0.06$, while the bright state (b) deviates from power law behavior.	47
4.13. Truncated power law fit of dim state of QE9.....	48

CHAPTER I

INTRODUCTION

1.1. Why Single Photons?

Quantum information technologies promise large impacts due to the wide implications of quantum computation and communication. Quantum computation would enable cracking of standard RSA encryption,¹ efficient simulation for materials or drug discovery.² Quantum communication in the form of quantum key distribution would yield secure transmission of encryption keys,³ while efficient transmission of qubits between systems would enable distributed quantum computing.⁴

Single photons offer a route to realize these technologies. Single photons could be used to efficiently perform searching or sampling problems.⁵ Single photons could also be used to implement universal quantum computing with linear optics⁶ if they possess high indistinguishability and the probability of having two photons emitted is low. Single photons are the natural messenger for quantum communication as they are highly mobile and stable over long distances by nature. Quantum key distribution has a relaxed requirement, needing only low two-photon probability with efficient single photon generation preferred. Performing quantum communication for distributed quantum computing may be the most challenging potential application with a requirement of strong coupling to a specific quantum computer, but perhaps achievable using highly tuned optomechanical structures.

1.2. Why Hexagonal Boron Nitride?

There are many types of single photon sources, however the most established still come with limitations. Spontaneous parametric down-conversion sources can have nice spectral properties, but they are stochastic, making on-demand photon generation difficult. Quantum dots can be bright and emit highly indistinguishable photons but can generally operate only at cryogenic temperatures. Single photon emitters (SPEs) in hexagonal boron nitride (hBN) can offer a solution to these problems because they are bright, photostable, and can have a Fourier transform-limited spectrum at room temperature. Moreover, due to its nanoscale thickness it offers a high degree of integrability with hybrid photonic or plasmonic structures for on-chip routing of single-photons.

The high brightness and photostability of these single photon emitters are crucial for use in many different quantum information technologies due to the desire for on-demand single-photon generation. This is important so that a user could deterministically prepare a desired quantum state to perform a desired operation at a high repetition rate. Example operations include entangling a pair of photons for quantum key distribution or preparing a many photon state to be sent through a linear-optical quantum computer.

Fourier-transform limited spectra are a crucial step towards demonstrating indistinguishable single photons that can be used in linear-optical quantum computers. Moreover, the room temperature demonstration of Fourier-transform limited lines suggests that these SPEs could operate without the typical cryogenic temperatures and the complex setups. This simplification would likely make these emitters easier to use than the current favorite, spontaneous parametric down conversion.

1.3. Limitations and how we tried to beat them

While hBN single photon emitters do have desirable brightness and can have very narrow spectral lines, there are difficulties facing their practical use. In contrast to individual linewidths, the spectral variation between single photon emitters is 200 nm.⁷ This makes indistinguishable photon generation difficult and limits the potential for on-chip integration because photonic or plasmonic structures must be tuned to individually identified SPEs. On-chip integration is further inhibited by the stochasticity of hBN emitter creation, meaning that photonic or plasmonic on-chip structures must be built around a specific SPE even without spectral concerns.

Experimental and theoretical evidence suggests that strain is a cause of wavelength variation in hBN SPEs.^{8,9} Thus, changes in wavelength could be due to bending that occurs on a thin hBN flake in the process of preparing samples for optical measurements. However, this wavelength variation is reduced to 30 nm,¹⁰ for emitters in thick bulk hBN that are less susceptible to bending due to their thickness. However, the thickness of those samples makes them less integrable with hybrid photonic structures. In order to take advantage of the integrability of a nanoscale structure while keeping a low wavelength variation, we searched for emitters in a more structurally robust hBN allotrope.¹¹ We show that emitters in this allotrope, called a boron nitride nanococoon, possess a wavelength variation of 39 nm - a factor of five reduction compared to thin hBN flakes.

Opportunities for controlled creation of hBN emitters are suggested by studies that show they tend to form at edges, grain-boundaries, or folds in hBN flakes.¹² A recent finding has shown that artificial folds can be leveraged to create arrays of hBN emitters,

however it requires a structured substrate and thin, flexible hBN which limits the usability of the technique.¹³ In order to address the challenge of deterministic creation of emitter in hBN with the greatest applicability, we used a focused ion beam to create edges on which single photon emitters could form.¹⁴ With our optimized process, we show that we can create sites with an average photon number under one with 31% yield – near the limit of a Poissonian process.

The work described in this dissertation is based largely on co-authored material. Chapter III contains published co-authored material with contributions from Andrew Blaikie, Aidin Fathalizadeh, David Miller, Fehmi S. Yasin, Kerisha Williams, Jordan Mohrhardt, Benjamin J. McMorran, Alex Zettl, and Benjamín Alemán. Chapter IV contains published co-authored material with contributions from Rachael Klaiss, Andrew Blaikie, David Miller, Viva Horowitz, and Benjamín Alemán.

CHAPTER II

MEASURING SINGLE PHOTON EMISSION: THE SECOND ORDER CORRELATION FUNCTION

2.1. Introduction

The key measurement needed for characterization and engineering of single photon emitting defects is a way to verify that a source of fluorescence is emitting single photons. Correlation functions offer a way to achieve this. Correlation functions have been a key tool to measure the properties of optical fields since Glauber formulated the full quantum theory for optical coherence in 1963.¹⁵ The first order correlation function, $g^{(1)}(t)$, is useful for determining fluorescence trajectories for measurements of lifetimes, for example, but are insufficient to determine many other properties. Crucially, the features distinguishing classical optical fields from quantum fields can only be found in a second order correlation function, $g^{(2)}(t)$, and higher orders. The second order correlation function is the key tool we use to identify and describe single photon emitting defects in hexagonal boron nitride.

A quantized electric field can be identified by antibunching at times near zero in the second order correlation function. This was first observed experimentally by Kimble et al.¹⁶ in 1977 following suggestions of Stoler¹⁷ in 1974. The phenomenon of antibunching occurs when the distribution of photons in time is sub-Poissonian, i.e. has a variance less than the mean photon number, a feature that is only possible with an

intensity probability distribution that is not positive semi-definite.¹⁸ It is that key feature that unambiguously shows that antibunching is a quantum effect.

More simply, one can think of a beam of single photons incident on a beam-splitter leading to two detectors. Each photon can only go to one detector in the absence of nonlinearities. Necessarily, this will exhibit antibunching since we have specified that we have a beam of single photons that follow each other after some finite amount of time has passed. Thus, a dip will be observed when measuring photon coincidences as a function of time in a second-order correlation measurement. The simplicity of the measurement combined with the unambiguity of the resulting antibunching dip as a quantification of photon number has enabled this measurement to emerge as the primary tool for identification of single photon emitters.

2.2. Mathematical modeling

In order to identify whether we have a single photon emitter, it is crucial that we normalize our $g^{(2)}(t)$ measurement so we can compare it against unbunched light and quantify various properties of the photon source. The normalization is simply the expected intensity of the light if the photons were randomly distributed across all time rather than arriving sequentially. We measure $g^{(2)}(t)$ by setting up two detectors in a Hanbury Brown-Twiss setup, and designate one of them as the start detector and the other as the stop detector. The start detector triggers a time-correlated single photon counter to start a timer when it detects a photon and the stop detector triggers the card to stop the timer. We can then log this start-stop time as an event on a $g^{(2)}(t)$ histogram labelled by the start-stop time measured. For this histogram of photon counts we have

δ/T bins, where δ is the bin width and T is the measurement time. We then have N_1 start counts evenly distributed across each bin. Each start count has equal probability of being stopped by each of N_2 stop counts. This leads to a normalization factor of $N_1 N_2 \delta / T$.¹⁹

The part of $g^{(2)}(\tau)$ that we most care about is its value at zero times, since that is where we expect to find the greatest antibunching and the critical information about the fluorescent source we probe. From a quantized description of the electric field one can obtain the following equation for $g^{(2)}(0)$ in terms of photon creation and annihilation operators,¹⁵ \hat{a}^\dagger and \hat{a}

$$g^{(2)}(0) = \frac{\langle (\hat{a}^\dagger)^2 \hat{a}^2 \rangle}{\langle \hat{a}^\dagger \hat{a} \rangle^2}$$

We can relate this to the variance of the field by using commutation operators and the definition of the number operator $\hat{n} = \hat{a}^\dagger \hat{a}$

$$V_n = \langle \hat{n}^2 \rangle - \langle \hat{n} \rangle^2 = \langle (\hat{a}^\dagger \hat{a})^2 \rangle - \langle \hat{a}^\dagger \hat{a} \rangle^2 = \langle (\hat{a}^\dagger)^2 \hat{a}^2 \rangle + \langle \hat{a}^\dagger \hat{a} \rangle - \langle \hat{a}^\dagger \hat{a} \rangle^2$$

Inserting this into our equation for $g^{(2)}(0)$ we obtain:

$$g^{(2)}(0) = \frac{(V_n + n)}{n^2} - 1$$

Assuming a Poissonian background, with variance equal to its fractional contribution to events measured squared, with b , s background and signal contributions,¹⁹ respectively:

$$g^{(2)}(0) = \frac{b^2/(s+b)^2 - n}{n^2} - 1$$

The $g^{(2)}(t)$ function we measure for single photon emitters is simply a model for the probability of the system to emit a photon, normalized to a random (time invariant) emission process. We model our single photon emitters as a three-level lambda system with the intermediate state exhibiting a long-lived nonradiative transition with

exponential decay from both the radiative and non-radiative excited states. Since this nonradiative transition doesn't contribute photons it necessarily reduces photon counts as time goes on, resulting in bunching at short times. This nonradiative transition is of variable strength so we include a parameter to account for the amount of bunching it generates.²⁰ Putting this together, we obtain:

$$g^{(2)}(t) = 1 - \rho^2 + \rho^2 \left[1 - (1 - a) e^{-\frac{|t|}{\tau_1}} + a e^{-\frac{|t|}{\tau_2}} \right]$$

Where a is the bunching amplitude due to the nonradiative state, τ_1 is the lifetime of the radiative state, τ_2 is the lifetime of the nonradiative state, and $\rho = 1 - g^{(2)}(0)$ with $g^{(2)}(0)$ as defined above for a Poissonian background.

2.3. Possible issues

A possible issue with reading photon number from $g^{(2)}(0) = \frac{1}{n} - 1$ arises when the intensity of multiple photon sources is not equal. Jungwirth explored this issue in his thesis as well.²¹ We can identify the value of $g^{(2)}(0)$ by considering our detection setup. Assuming we have contributions from n distinct single photon emitters and a Poissonian background we need to consider all $(n + 1)^2$ possible ways a start and stop can be triggered by these $n + 1$ sources. However, we must also take into account that a single photon emitter can't trigger a start and stop at the same time. With b the intensity of the background, s_i the intensity of each single photon emitter, and ξ the sum of the intensities we obtain:

$$g^{(2)}(0) = \frac{b^2}{\xi^2} + \sum_{j \neq i=1}^n \sum_{i=1}^n \frac{s_i s_j}{\xi^2} + \sum_i^n \frac{s_i b}{\xi^2}$$

From this, one can see that for two emitters of equal intensities one recovers the familiar $g^{(2)}(0) = 1 - \frac{1}{2} = 0.5$. On the other hand, if one is three quarters of the intensity of the other, one obtains $g^{(2)}(0) = 0.24$. This can be contrasted with the case with one single photon emitter and a background that is three quarter its intensity which results in $g^{(2)}(0) = 0.43$. It is immediately obvious that the standard zero-background measure of $g^{(2)}(0) = 1 - \frac{1}{n}$ is insufficient to identify the presence of an isolated single photon emitter if variation in brightness is possible. Therefore, interpretation of $g^{(2)}(0)$ must incorporate other characterization methods like spectra or polarization for reduced ambiguity. Regardless, $g^{(2)}(0)$ is still a key measure of a fluorescent source for determining its single photon purity for use in quantum information applications.

2.4. Bridge

With this chapter we have established a metric to determine whether a source of fluorescence is a single photon emitting defect. This tool enables us to search for these defects, characterize them, and engineer them. While there are other tools that must be employed to better understand the physics and chemistry of single photon emitting defects in hexagonal boron nitride, none are as crucial for determining whether the thing we are investigating may be useful for quantum information technology applications.

CHAPTER III

SINGLE PHOTON EMITTERS IN BORON NITRIDE NANOCOCOONS

This chapter contains previously published co-authored material; it has been reproduced with permission from: J. Ziegler, A. Blaikie, A. Fathalizadeh, D. Miller, F. S. Yasin, K. Williams, J. Mohrhardt, B. J. McMorran, A. Zettl, B. Alemán, “Single-Photon Emitters in Boron Nitride Nanococoons.” *Nano Letters*. 2018, 18 (4), 2683–88. Copyright 2018 American Chemical Society.¹¹ This article can be accessed [here](#). In this work, I contributed to designing the research, performing the research, analyzing the data, and writing the paper.

3.1. Introduction

Solid state sources of single photons have broadly impacted the development of quantum technologies due to their robustness to ambient conditions^{22–24} and ease of integration with on-chip devices²⁵. These attributes have allowed the realization of applications from quantum computers²⁶ and entanglement between remote qubits²⁷, to thermometry²³ and imaging²⁴ in living biological systems. Recently, single-phonon emitters (SPEs) have in two-dimensional (2D) hexagonal boron nitride (hBN) have attracted significant attention because of their extreme brightness, photoluminescence (PL) stability^{28–35}, and robustness to harsh chemical and temperature conditions^{30,36}. In addition, their nanometer-scale thickness allows for strong coupling to the environment or to photonic structures. However, hBN SPEs suffer from an emitter-to-emitter

wavelength variability of 200 nm³⁰, which proves detrimental to many applications in photonics, quantum information, and fluorescence imaging because of a strict reliance on a fixed and well-defined wavelength. Experimental evidence and theoretical analysis indicate that strain is an important contributor to this wavelength variation^{30,33}. Therefore, the variation can originate from morphological features like folds and wrinkles, or incidental bending or tensioning of the hBN sheet—factors that are challenging to control.

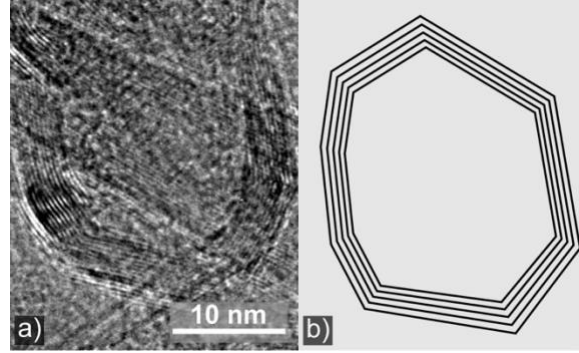


Figure 3.1. (a) High resolution transmission electron microscopy (TEM) image of a BNNC on a BNNT showing its walls and hollow interior. (b) A sketch of a BNNC cross section emphasizing the locally flat faces.

Because of the otherwise excellent properties of hBN, a means to reduce the strain-driven wavelength variability would propel the potential of the hBN SPE. One solution would be to utilize a geometry that is resistant to bending. Thick, bulk hBN samples have a large bending stiffness, and SPEs in such samples do possess a narrower emission wavelength range (~ 30 nm³⁷) relative to thin hBN sheets. However, this tighter emission range broadens considerably when the thickness of the sample is reduced to less than 100 nanometers³⁰—even with the small lateral scale of an hBN nanoflake. So, despite the improved SPE emission properties of bulk hBN, these properties cannot be combined with the desirable benefits of a nanoscale structure.

The boron nitride nanococoon (BNNC) is a ball-like, zero-dimensional (0D) BN allotrope that possesses both a nanoscale size and a stable, rigid mechanical structure.

The BNNC—which is structurally similar to a carbon buckyball fullerene³⁸—is composed of fully closed, nested BN polyhedra and provides more rigidity and fewer motional degrees of freedom than a 2D flake. This resistance to bending would result in lower wavelength variation of SPEs in this nanostructure. In addition to bending resistance, the BNNC also has a nanometer size (~ 1- 100 nm) which would allow embedded SPEs to retain the efficient coupling of 2D hBN and to serve as sensitive probes of small systems. Critically, the BNNC has facets—consisting of many flat, stacked layers or walls of BN (see Figure 3.1)—that possess a local crystal structure identical to 2D and 3D hBN^{39,40}. This structure imparts a large bandgap^{41,42}, as seen in other BN allotropes, and therefore permits the formation of deep-bandgap visible-range SPEs.

Despite the potential for BNNCs to support SPEs with a more consistent, well-defined emission wavelength and the advantages of its nanoscale structure, the BNNC has yet to be investigated as a source of SPEs. Here, we examine a purified sample of BNNCs for the PL signatures of SPEs, and determine if the prospective SPEs possess reduced emission wavelength variation. By using confocal optical microscopy, we discover bright, stable SPEs that emit in the visible range and are active at room temperature and in air. These SPEs are stable over many days of continuous probing, and, most notably, can possess a wavelength variation of 39 nm. By cross-correlating confocal optical microscopy with high-resolution electron microscopy, we determine that the SPEs exist in isolated BNNCs and, more often, in large aggregates of composite BNNC material.

3.2. Methods and Materials

The BNNCs used in this study were grown from boron feedstock in an inductively-coupled plasma at high pressure⁴⁰. This commercially scalable process produces a mixture of BNNCs and BN nanotubes (BNNTs), but was tuned to preferentially produce BNNCs. The use of a boron source material minimized 2D or bulk hBN material in the synthesis product. The synthesis process also created boron nanocrystals, some of which were encapsulated by the BNNCs. We used a nitric acid treatment to remove these impurities. BN's excellent inertness⁴³ protected the material from oxidative damage of the acid.

After treatment in nitric acid, the material was suspended in ethanol, sonicated, filtered at 200 nm, and resuspended. Filtering helped remove larger assemblages of BNNC/BNNT or potential hBN sheets. For transmission electron microscopy (TEM) studies, the BNNCs were then drop-casted onto a lacey carbon TEM grid. This dispersion decreased the density of material to make it more likely to find isolated SPEs and to allow for cross-correlation characterization of the SPE host material. A TEM image of a BNNC can be found in Figure 3.1 (a) with a sketch of the cross-section in Figure 3.1 (b). In order to create and increase the density of SPE defects, we used an FEI Helios dual-beam focused ion beam (FIB) and scanning electron microscope (SEM) to selectively irradiate the sample with 10 keV gallium ions at a dose of 10^{-14} C/ μm^2 . Subsequently, we annealed the samples in argon at 1 Torr and 750° C for 30 minutes³⁵. In order to expedite sample processing, some samples were only annealed, which resulted in a lower defect density and defects with diminished stability³⁵.

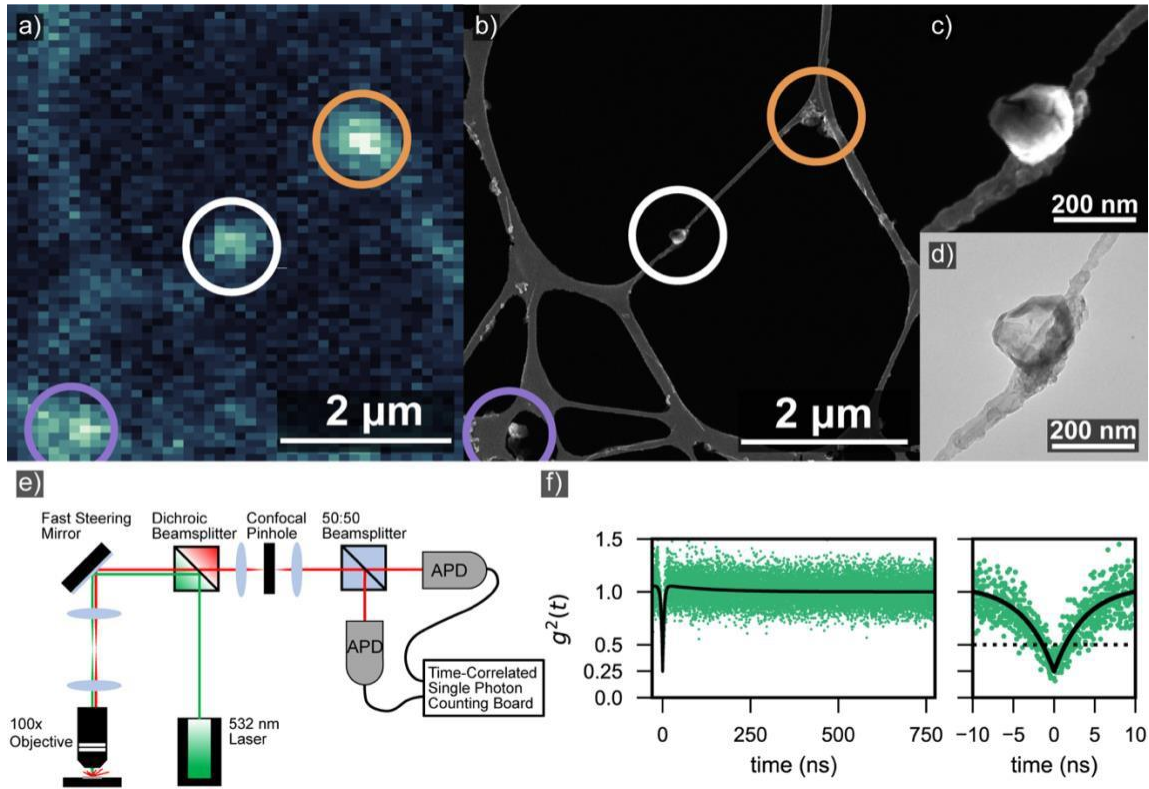


Figure 3.2. (a) Confocal image of a BNNC that hosts a SPE with an arbitrary intensity scale. The bright spot circled in white is a SPE hosted by a single BNNC. The bright spots circled in color were used as references to help correlate confocal and SEM/TEM images. (b) Low magnification SEM image of the BNNC that hosted a SPE on lacey carbon. (c) High magnification SEM image of the same BNNC on lacey carbon (d) TEM image of the BNNC on lacey carbon showing the hollow interior and thick walls. (e) Sketch of our confocal microscope optical setup, with two avalanche photodiodes in a Hanbury-Brown-Twiss setup for $g^2(t)$ measurements. (f) $g^2(t)$ for a single BNNC showing that $g^2(0) = 0.25$ – proving it is a SPE.

We used a custom-built scanning confocal microscope to generate two-dimensional fluorescence images of our samples. From these images, we identified areas with localized PL as potential SPEs. Typical scan areas were $10 \mu\text{m} \times 10 \mu\text{m}$. A schematic of this optical setup can be found in Figure 3.2 (e). This setup uses a 100X N.A.=0.7 objective to focus light on our sample, a mode-filtered 532 nm laser for excitation, and avalanche photodiodes (APDs) for single-photon counting. The positioning of the laser focus has closed-loop control and nanometer-scale resolution in

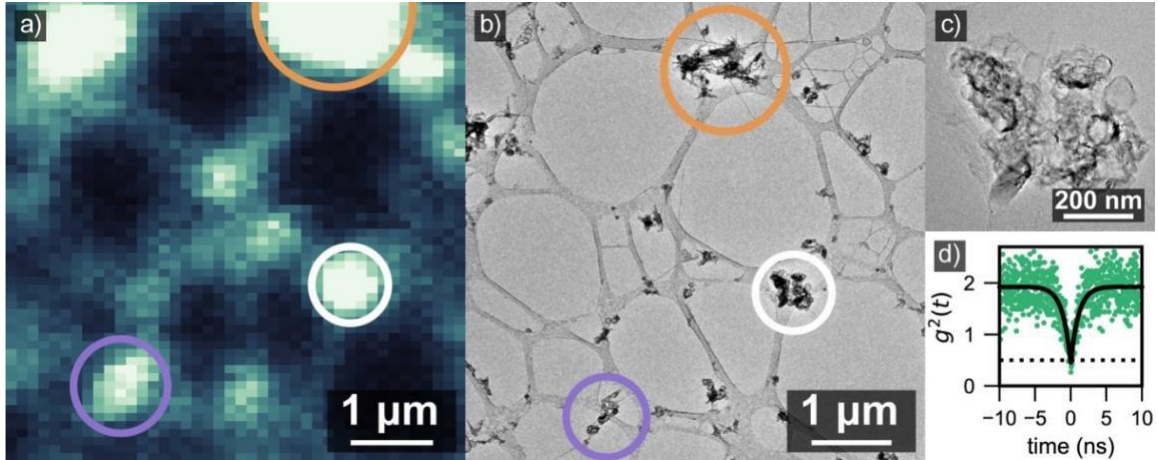


Figure 3.3. (a) Confocal image of aggregated BN nanomaterial on lacey carbon with an arbitrary intensity scale. The bright spot circled in white is an SPE hosted by a cluster of BNNC. The bright spots circled in color were used as references to help correlate between confocal and SEM/TEM images. (b) Low magnification TEM image of aggregated BN nanomaterial on lacey carbon. (c) High magnification TEM image of the SPE-hosting aggregate material showing the large number of BNNCs present. (d) $g^2(t)$ for this material with $g^2(0) = 0.44$ – proving it is a SPE.

all three dimensions. When probing single SPEs, we implemented a PL feedback loop to compensate for sample drift. All measurements were taken in air and at room temperature. For the majority of our imaging, we kept the excitation power low ($\sim 20 \mu\text{W}$) to minimize damage to the lacey carbon.

We identified SPEs and their hosts by using a combination of confocal microscopy, time-correlated single photon counting, and high-resolution electron microscopy. A typical confocal image of the BNNC material on a TEM grid is shown in Figure 3.2 (a); an SPE is circled in white. We identified PL sources as SPEs—that is, whether they emit single photons at a time—by measuring the second-degree correlation function, $g^2(t)$, with a Hanbury-Brown-Twiss photon detection setup integrated with our scanning confocal microscope (see Fig. 3.2 (e)). To determine the morphology of the SPE host material, we correlated confocal images with SEM and TEM images. The grid lattice and local

features of the lacey carbon of the TEM support facilitated imaging in the same regions for cross-correlation. An SEM/FIB was used for coarse identification of the material, as shown in Figure 3.2 (b), (c). For finer characterization, we used high-resolution TEM (obtained with an FEI Titan operated at 300 keV and an FEI Tecnai operated at 80 keV.) A representative TEM image of a single BNNC is shown in Figure 3.1 (a).

3.3. Results and Discussion

Confocal imaging revealed areas of bright, localized fluorescence. Three such bright regions are indicated by circles in Figure 3.2 (a) and 3.3 (a). SEM and TEM imaging (discussed in more detail below) shows that these same optically bright regions contain large amounts of BN material, as shown in Figure 3.2 (b) and 3.3 (b). Comparing the confocal and SEM images, we see some fluorescence from the lacey carbon support, but the intensity of this fluorescence is far below the signal in regions containing BNNCs. By measuring $g^2(t)$ of localized PL sources, we detected the presence of numerous SPEs in the BNNC material. The $g^2(t)$ data for the PL source pictured in Figure 3.2 (a)-(d) is shown in Figure 3.2 (f). We fit our $g^2(t)$ data to a model for a three-level system with a long-lifetime non-radiative transition: $g^2(t) = 1 - (1 + a)e^{-\frac{|t|}{\tau_1}} + ae^{-\frac{|t|}{\tau_2}}$ where τ_1 is the radiative lifetime, τ_2 is the non-radiative lifetime, a is the amplitude of bunching. This model of a three-level-system is consistent with our data and has also been used to describe SPEs in hBN^{28,37}. We found the dip at zero time-difference for this emitter to be $g^2(0) = 0.25$ – well below the 0.5 threshold for a single photon source. In total, we found 23 SPEs, with excited state lifetimes in the range 0.8-11 ns, and bunching amplitudes from 0 to 1. A large bunching amplitude (~ 1) indicates a long-lived non-radiative decay

pathway²⁹. In addition, we found several dozen separate instances of anti-bunched PL (*i.e.* $0.5 < g^2(0) < 1$.) We found roughly one SPE per $50 \mu\text{m} \times 50 \mu\text{m}$ area.

We further characterized the SPEs by measuring their PL spectra at room temperature. These measurements were performed in a commercial Witec Raman Spectrometer. Representative spectra are shown in Figure 3.4 (a); these spectra have a strong, sharp peak and a broader, red-shifted shoulder which resemble the zero phonon line (ZPL) and phonon side band, respectively, expected for a solid-state color center (additional spectra can be found in section 3.5) Across 12 distinct SPEs with strong ZPLs, we found an average ZPL of 578 ± 14 nm with a total range of 39 nm, which is a factor of five lower than the range of 200 nm for emitters in few-layer hBN^{30,34}. The range seen in BNNCs is closer to the 30 nm ZPL range of SPEs in bulk hBN³⁷, and some measured spectra have ZPLs that are tightly grouped about an emission line at 567 nm. The deviation within this group (composed of all emitters below the median of 575.7 nm) is about ± 3 nm or a factor of 33 lower than few-layer hBN, suggesting a possible route toward further wavelength stability in this system. We can understand the small variability by considering the increased rigidity of the cocoon structure, which prevents strain-induced wavelength shifts, much like what occurs in bulk hBN. The phonon sideband is separated from the ZPL by 158 ± 15 meV—roughly consistent with 2D and bulk hBN SPEs^{28,30,31,37}. This energy separation is close to a peak in hBN’s phonon density of states at 165 meV⁴⁴, which provides evidence that the crystal structure of the BNNC near the SPE is similar to 2D and bulk hBN, as illustrated for the BNNC in Fig. 3.1 (a). Despite the similarities to bulk hBN, the BNNC spectra are blue-shifted by ~ 20

nm relative to those in bulk hBN, a shift that may be caused by the different strain and bonding environment of the BNNC.

To gain further understanding of the SPEs excitation and emission properties, we examined the polarization dependence of their PL intensity. We found the two-lobed shape typical of an optical dipole as well as misaligned excitation and emission dipoles. We confirmed the dipole characteristic of these emitters by fitting the PL intensity vs. θ data to the $\cos^2\theta$ shape expected for a linearly polarized dipole—see Figure 3.4 (c). Misalignment between emission and excitation dipoles was common although

the angle between them varies. This misalignment can be attributed to indirect excitation of the emitter through a higher-lying state. Such misaligned excitation and emission optical dipoles are also found for SPEs in other BN allotropes^{29,45}.

We determined the brightness of these SPEs by measuring the PL intensity at various levels of incident power, as seen in Figure 3.4 (b). The polarization was adjusted in these measurements in order to maximize the PL intensity. We fit the data using a first-order saturation model³⁷, with an equation of the form $I(P) = I_{\infty}P/(P + P_{sat})$. For the

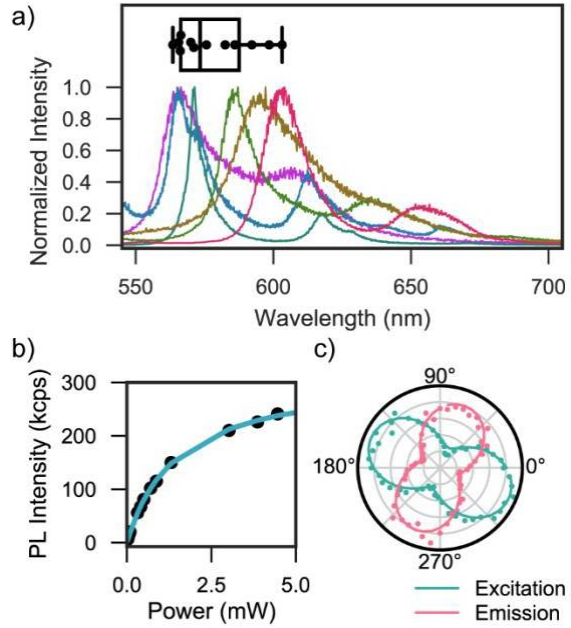


Figure 3.4. (a) Representative spectra for different SPEs with a range from 564-603 nm, normalized for clarity. The box and swarm plots summarize the ZPL data of spectra obtained. (b) PL intensity vs Power curve showing $I_{\infty} = 320$ kcps and $P_{sat} = 1.5$ mW. (c) Polarization vs. PL intensity with a shape characteristic of a linearly-polarized optical dipole and misalignment between the excitation and emission dipole.

brightest emitter suspended on lacey carbon, the saturation intensity, I_{∞} , was 318 kcps and the saturation power, P_{sat} , was 1.48 mW.

The saturation intensity of our brightest emitter is an order of magnitude less than the 4000 kcps reported brightness of SPEs in 2D hBN^{28–35}. We can partially attribute the dimmer emission to a lower collection efficiency in our optical setup. At the same incident power, we found that a SPE in an hBN flake—prepared from commercially available hBN nanoflakes (Graphene Supermarket)—had a PL intensity of 500 kcps while a SPE in a BNNC had a PL intensity of 100 kcps. Accounting for the inefficiencies in our optical setup, we find that SPEs in BNNCs are roughly a factor of five dimmer than those in hBN flakes. The remaining difference in brightness may be due to the low layer number of these structures, local crystalline damage, or the sub-wavelength size and high index of refraction of the BNNCs^{46–48}.

During optical characterization, we noticed a reversible reduction in brightness of some SPEs that remained stable on a time scale of minutes to hours. After further investigation, we found that extended illumination of some SPEs at high incident powers (*i.e.* at or above saturation, 1.5 mW) could induce a change from a bright to a dim state, with the overall PL intensity dropping by over 60%. This dimming was accompanied by a dramatic reduction of the ZPL intensity by over 80% (Figure 3.5 (a)). In addition, we measured $g^2(t)$ for both the bright and dim state and found a reduction in lifetime from 2.59 ns to 0.826 ns—shown in Figure 3.5 (b) and (c), respectively. However, the SPE antibunching behavior persisted in the dim state. The lifetime change accompanied by the change in spectrum seems to suggest a change in the strength of phonon coupling or other non-radiative decay pathways.

The photoinduced changes we observed have pronounced differences from those seen in 2D hBN³². In 2D hBN, photodynamic processes were only observed under 405 nm illumination and primarily consisted of spectral diffusion, sometimes accompanied by dimming of the defect. In contrast, we observed dimming without spectral diffusion under 532 nm illumination. Also, the photoinduced changes in 2D hBN were stable on time scales of seconds, whereas we observed stability on the order of hours to days. It is possible that the photo-induced

dimming and lifetime changes are due to a similar mechanism as proposed for 2D hBN, such as changes in the charge state of the SPE or surface desorption of oxygen³². However, the differences suggest that the photodynamics are unique to the BNNC structure, and could be due to mechanical buckling or photochemical reactions at the highly strained and reactive edges of the BNNCs.

We used confocal and SEM/TEM cross-correlation to ascertain the morphology and identity of the SPE host material. Examples of these correlations can be found in Figures 3.2 and 3.3, where the PL source circled in white is an SPE and the areas circled

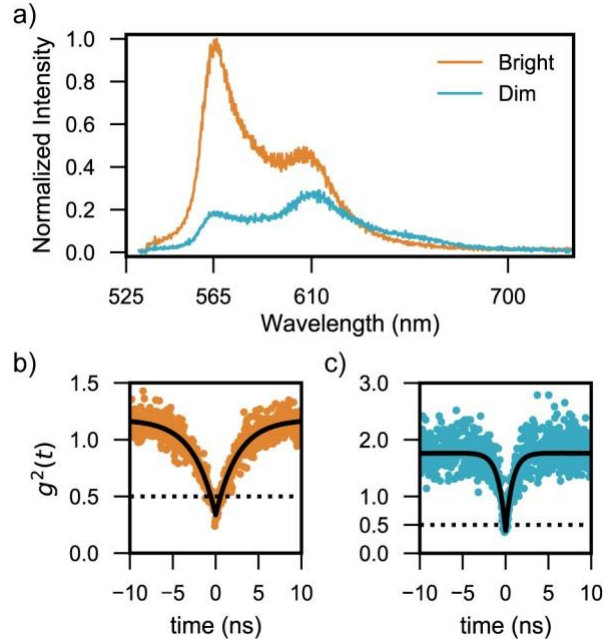


Figure 3.5. (a) Spectra for the bright and dim state showing a reduction in ZPL and overall PL intensity without a corresponding change in wavelength, with intensity normalized to the ZPL of the bright state. (b) $g^2(t)$ for the bright state – the lifetime was 2.59 ns and $g^2(0) = 0.34$. (c) $g^2(t)$ for the dim state - the lifetime was 0.83 ns and $g^2(0) = 0.38$.

in purple and orange are local features used to facilitate cross-correlation between optical and electron microscopes. The source of localized PL shown in Figure 3.2 (a) (white circle) possessed an anti-bunching correlation of $g^2(0) = 0.25$, firmly establishing the emitter as an SPE. SEM and TEM images of the region near this SPE (Figure 3.2 (b)-(d)) show a single particle of diameter ~ 150 nm. The SEM shows the particle has some depth (*i.e.* it is not flat) and has sharply angled facets in all three dimensions. TEM of the particle shows dense material (darker) at the edges of the particle and less material (lighter) at its center, consistent with the geometry of a hollow BNNC. The structure of a nanococoon and its sharply angled facets can be more clearly seen in Figure 3.1(a), where the walls of the BNNC are resolved. The BNNC cluster seen in Figure 3.3 (c) also shows the hollow-core and dense wall structure of nanococoons. Based off this collective evidence, we conclude that the SPE highlighted in Figure 3.2 exists within a single BNNC. The majority of the SPEs were found in aggregated mixtures of BNNC and BNNT material primarily composed of nanococoons (see Figure 3.3 (b)-(c) and Figures 3.7, 3.8, 3.9 (b)-(d).)

Although the material is a mix of BNNCs and BNNTs, we note that isolated or bundled nanotubes lacked PL of any kind. This absence of PL from BNNTs agrees with other searches for SPEs in composite BN nanomaterial containing nanotubes⁴⁹. Therefore, we suspect the SPEs were hosted by BNNCs alone. The apparent preference of SPEs to form in aggregated material is likely due to the larger amount of material available to host the emitter. Isolated BNNCs that possess an SPE also tend to be larger (~ 100 nm), thereby increasing the likelihood of containing an SPE. We point out that in all our TEM observations, we did not see any 2D or 3D hBN. Taken together, in addition

to the noted differences in optical properties, we conclude that BNNCs are the hosts of all the SPEs measured in this work.

3.4. Conclusion

In this work, we have discovered bright, visible wavelength SPEs in a nanometer-scale BNNC structure. These new SPEs were optically active under ambient conditions, demonstrated stability over several days, and were found both in large isolated BNNCs and in clusters of BNNCs. While the lifetime, brightness, and PL stability of this SPE is similar to those in 2D hBN, it possesses one notable difference: its wavelength variation is a factor of five smaller than SPEs in 2D hBN. This discovery advances the development of the ultra-bright, stable solid-state single photon sources for quantum information, biological imaging, and photonics. Because the BNNCs can be synthesized in large quantities⁴⁰, they are viable for industrial-scale implementation. Because of their small size and emission wavelength stability, BNNCs can be incorporated into photonic structures, such as waveguides and photonic crystal cavities, that are nanoscale and designed around well-defined wavelengths. These same properties, in addition to the SPE's extreme brightness and established ease of chemical functionalization^{50,51}, make the BNNC ideal for tagging and tracking applications within living cells. The BNNC's closed structure may make the SPE wavelength sensitive to thermal strain, suggesting the use of BNNCs as a nanoscale temperature probe. The bright/dim photo-switching behavior of the SPEs, if due to interactions of the BNNC surface with the surrounding environment, could be combined with surface functionalization to enable a broad range of optically detected sensing applications.

3.5. Supplementary Information

All Spectra Obtained from Single Photon Emitters

Figure 3.6 shows the full spectra for each SPE found in BNNCs. This data is summarized in Figure 3.4 in section 3.3.

Characterization of Single Photon Emitter Host Material

The zeroth step needed to cross correlate confocal and electron microscope images was to identify which square on the TEM grid our SPE was located and roughly the region within that square. Given our mesh size, that gave an area $<250\mu\text{m}^2$ to search. After identifying the square where the SPE was located, cross-correlation of confocal microscope images with scanning and tunneling electron microscope (SEM and TEM) images was performed by identifying bright features near to the SPE in images taken with a confocal microscope, identifying those sources of PL in SEM, then using those features as roadmaps to enable us to find the SPE in the TEM. These successive steps were often necessary due to the small field of view in the TEM which makes navigation of the sample difficult. Figures 3.7, 3.8, and 3.9 in this section as well as Figures 3.2 and 3.3 in the previous section show examples of how this correlation between the three microscopes is performed. These SPEs shown were also the emitters for which spectra was obtained.

The TEM imaging of Figure 3.7, 3.8, and 3.9 was performed at 300 keV, but the energy was lowered to 80 keV for later imaging to prevent damage to the BNNC material and the lacey carbon substrate.

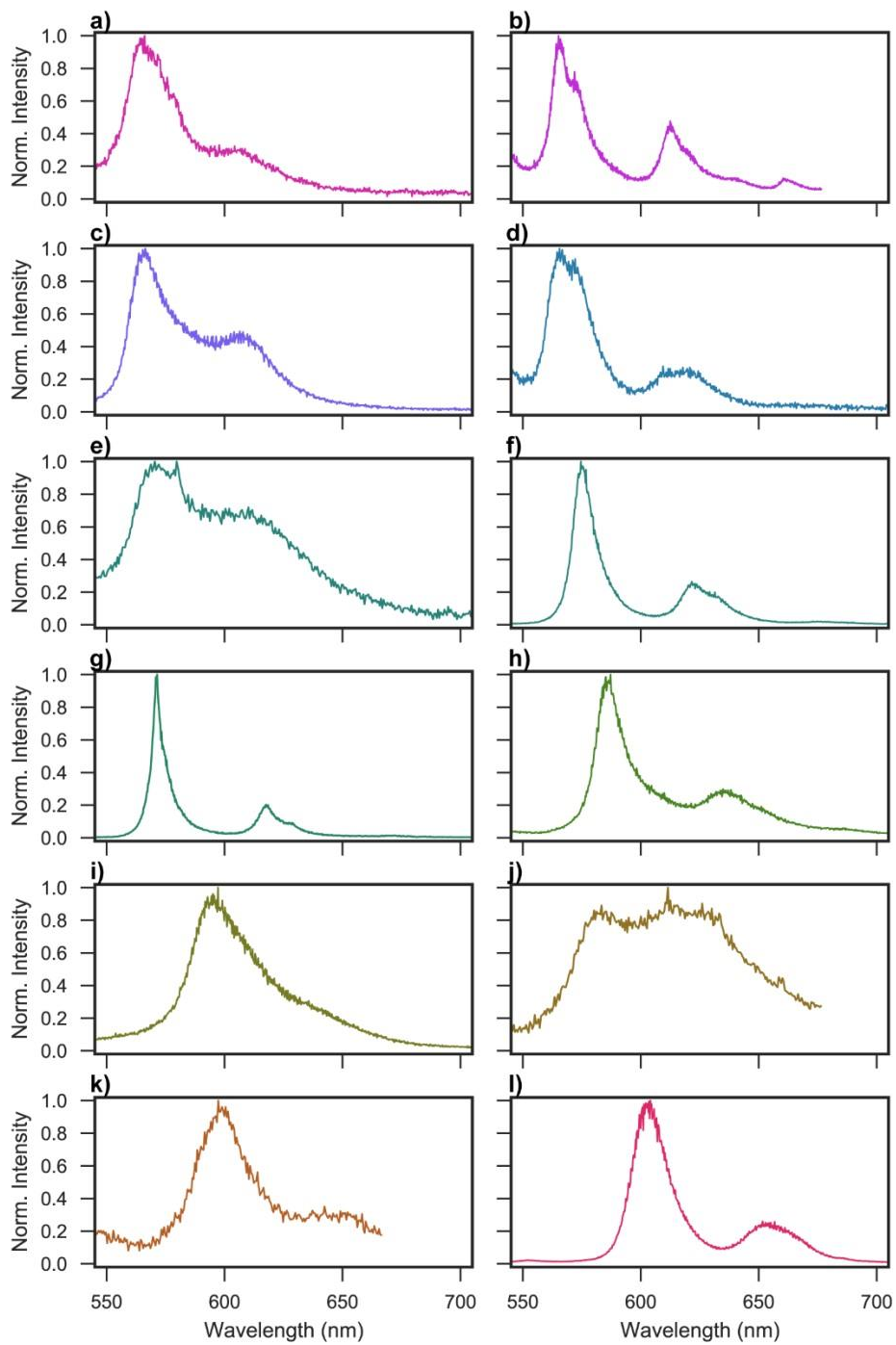


Figure 3.6. (a)-(l) All spectra obtained from SPEs found in BNNCs on lacey carbon. All of these spectra were considered when calculating the average zero phonon line and phonon sideband (PSB) of the BNNCs.

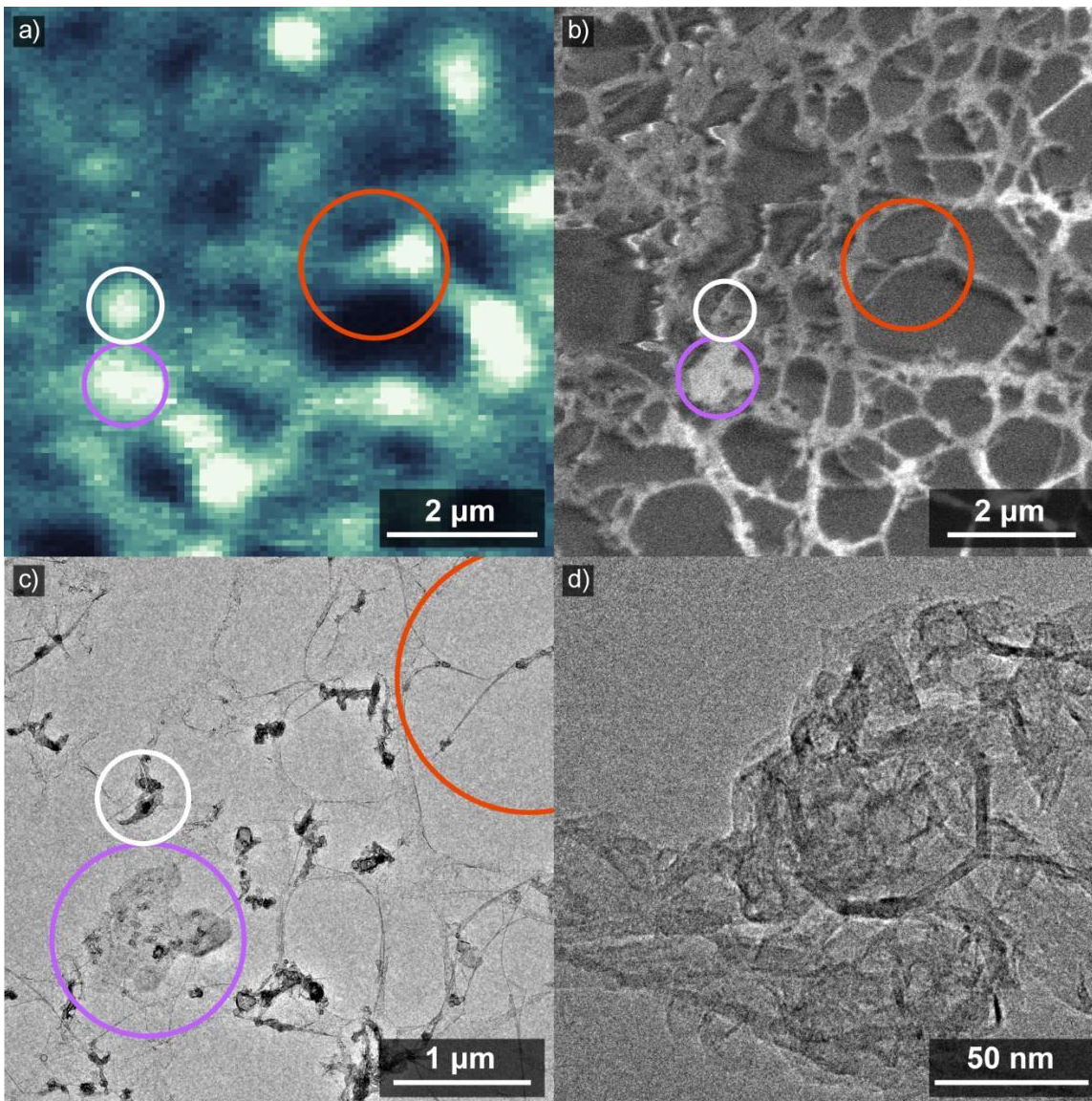


Figure 3.7. (a) Confocal image of a sample, with the SPE that exhibited photodynamics circled in white, and material used to correlate confocal images with SEM/TEM images circled in purple and orange. (b) SEM image of the same area of the sample. (c) Low magnification TEM image of the same area. (d) High magnification TEM image of the SPE showing the large amount of BNNCs present.

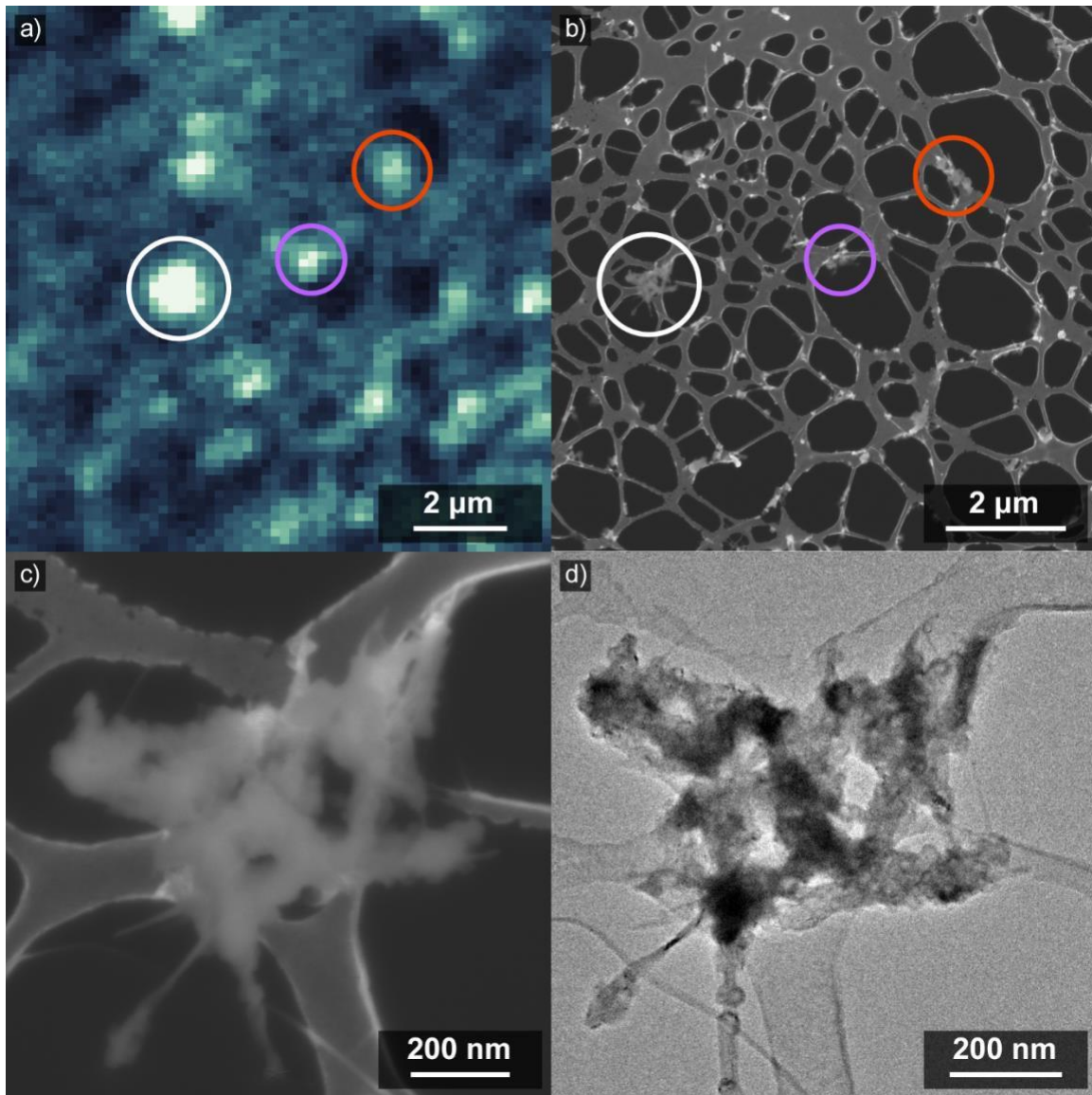


Figure 3.8. (a) Confocal image of a sample, with a SPE circled in white, and material used to correlate confocal images with SEM/TEM images circled in purple and orange. (b) Low magnification SEM image of the same area of a sample. (c) High magnification SEM image of the SPE. (d) High magnification TEM image of the SPE showing the large amount of BNNCs present.

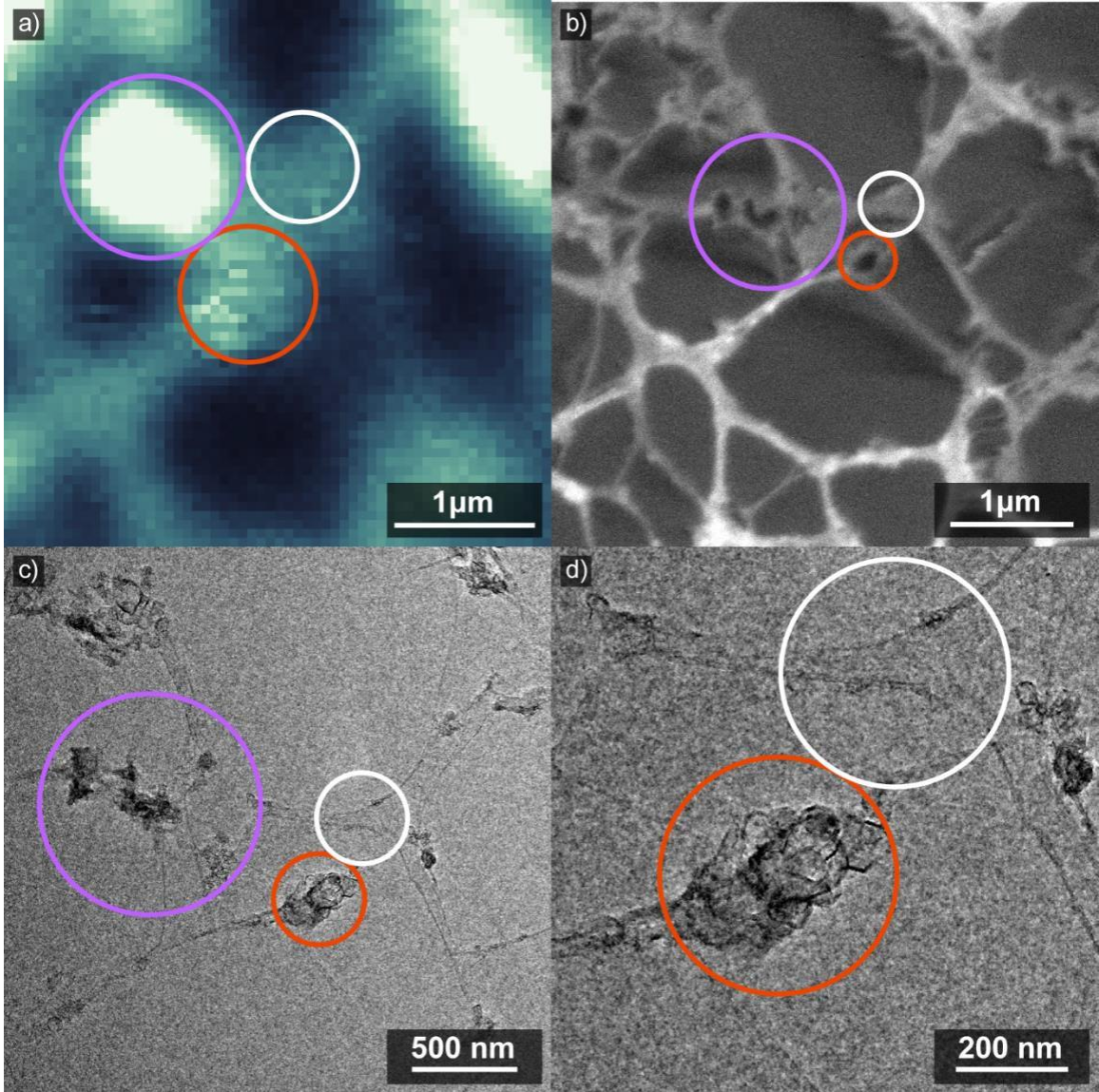


Figure 3.9. (a) Confocal image of a sample, with an SPE circled in white, and material used to correlate confocal images with SEM/TEM images circled in purple and orange. (b) SEM image of the same area of the sample. (c) Low magnification TEM image of the same area. (d) Higher magnification TEM image of the SPE showing the large amount of BNNCs present.

3.6. Bridge

In this chapter I have described work done characterizing single photon emitters found in a nanoscale allotrope of hexagonal boron nitride in which single photon emitters had not previously been found. The characterization skills I developed in the course of performing this research in combination with the greater understanding of single photon emitters in hexagonal boron nitride I gained were of tantamount importance for my ability to execute the work describe in the following chapter. I used all of the skills and knowledge learned performing the work described here and built on them by learning new characterization and fabrication skills while continuing to advance my understanding of single photon emitters in hexagonal boron nitride.

CHAPTER IV

DETERMINISTIC QUANTUM EMITTER FORMATION IN HEXAGONAL BORON NITRIDE BY CONTROLLED EDGE CREATION

This chapter contains previously published co-authored material; it has been reproduced with permission from: J. Ziegler, R. Klaiss, A. Blaikie, D. Miller, V. Horowitz B. J. Alemán, “Deterministic Quantum Emitter Formation in Hexagonal Boron Nitride via Controlled Edge Creation.” *Nano Lett.* 2019, 19 (3), 2121–2127. Copyright 2019 American Chemical Society.¹⁴ This article can be accessed [here](#). In this work, I contributed to designing the research, performing the research, analyzing the data, and writing the paper.

4.1. Introduction

Sources of single photons are a key component of many emerging quantum information technologies such as quantum computation, communication, and sensing.^{52–54} However, the more commonly used quantum emitters (QEs), such as cold atoms and spontaneous parametric down-conversion sources, require complex setups that limit their viability for widespread use. In contrast, solid-state QEs require significantly simpler setups because they can operate in ambient conditions.^{23,55} This attribute, combined with the possibility of high quantum efficiency^{56–58} and integrability with on-chip devices,^{59,60} suggests them as the ideal class of QEs for large-scale implementation of quantum information technologies.

Recent studies have discovered that hexagonal boron nitride (hBN), a large-bandgap 2D material, possesses QEs that are ultrabright and stable under ambient conditions.^{28,30,31,35,36,49,61–63} Moreover, because of hBN's atomic-scale thickness and extreme mechanical strength,⁶⁴ its QEs will couple strongly to photonic, plasmonic, and optomechanical modes, making them especially useful for hybrid quantum devices. However, to reliably integrate hBN QEs into these hybrid devices, a nanofabrication method to control both the creation and location of the QE (*i.e.* deterministic creation) is desperately needed. It has been observed that QEs tend to occur stochastically at edges or regions of high curvature,^{31,35} suggesting two routes toward deterministic creation of QEs in hBN. Recently, hBN QEs were created by inducing curvature with nanopillars.^{49,63} This technique achieved a yield of single QEs that is promising (~10%),⁶³ but the technique's potential for integration is significantly limited because it requires a structured substrate and thin hBN material.

In this letter, we propose and demonstrate a method to deterministically create QEs through the creation of edges in hBN. We create these edges by patterned milling of hBN using a gallium focused ion beam (FIB). By optimizing the milling and annealing^{28,30,35} parameters, we obtain a 31% yield of single QEs. We also explore morphology dependence of QE formation and find that they form best with uniform milling on relatively smooth CVD hBN. Our technique dramatically broadens the scope of applications of these QEs due to its high-yield and versatility, being independent from a structured substrate.

4.2. Results and Discussion

To create QEs in our hBN via edge creation, we transfer few-layer CVD hBN (Graphene Supermarket) onto SiO₂ and then use FIB to mill holes into the hBN, thereby forming edges at the hole perimeter. We do not perform an additional irradiation to activate QEs. The required dose to remove hBN material was in the range 10⁻¹³ C/μm² to 10⁻¹⁰ C/μm², with beam energies from 5-30 keV. Initial tests showed that energies of either 10 or 20 keV and milling doses of 1pC/μm² were close to optimum for see QE creation, as inferred by $g^2(0) < 0.5$ (see Figure 4.1b), so we studied two near-optimal conditions within this parameter range in greater depth. In one region of our sample (Region 1), we used the FIB milling conditions of 10 keV and 1 pC/μm², while in another region (Region 2) we used 20 keV and 10 pC /μm². In order to generate a high density of single, optically addressable QEs with enough perimeter for QEs to form, we FIB patterned arrays of 500 nm diameter circular holes with a center-to-center separation of 1 μm in each region. An atomic force microscope (AFM) image of these holes is shown in Figure 4.1(a), where the FIB was operated at 20 keV and 10pC/μm². The depth of the holes for this FIB condition was approximately 4 nm or 12

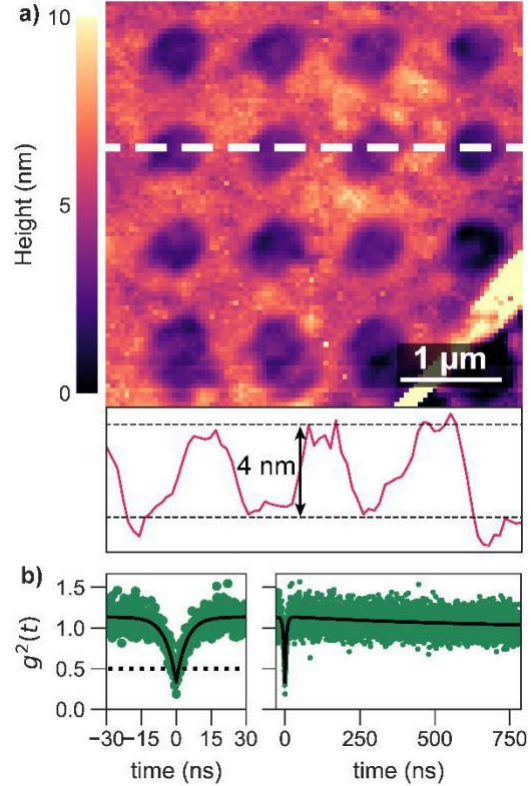


Figure 4.1: (a) AFM image of a FIB milled region of hBN, with a line cut shown below. (b) Example of $g^2(t)$ data for a single QE in Region 2 showing $g^2(0) = 0.33$, well below the antibunching threshold for a single QE. (left) 60 ns time window centered about $t = 0$. (right) 800 ns window of the same data.

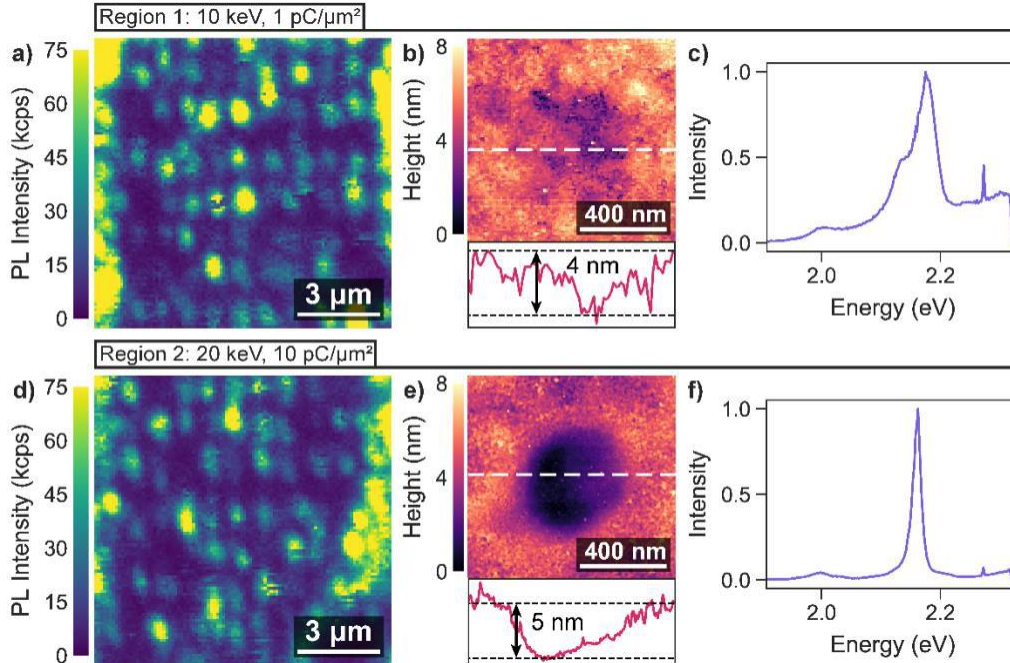


Figure 4.2: Confocal, AFM and representative photoluminescence spectra for QEs made with various FIB parameters. Top Row (Region 1): Low dose, low energy. Bottom row (Region 2): High dose, high energy. **(a)** Confocal scan showing high QE visibility. **(b)** AFM image showing rough, non-uniform milling **(c)** Representative photoluminescence spectrum showing a single emission line with a broad background. **(d)** Confocal scan showing high QE visibility. **(e)** AFM scan showing uniform milling and smooth sidewalls. **(f)** Representative photoluminescence spectrum showing a QE spectrum with low background.

hBN atomic layers. After milling, hBN flakes were annealed in oxygen at 850° C. This process serves to activate QEs^{28,30} while simultaneously removing carbon deposited by the FIB or residual organic material. This annealing step is usually performed in an inert (argon or nitrogen) environment,^{28,30,31,35,61} but annealing in oxygen typically doesn't affect QEs in hBN.³⁰ Although we are reporting results from CVD hBN, we also tested exfoliated hBN (HQGraphene) but the samples appeared to have a very high native defect density, which frustrated efforts to characterize single QEs (see section 4.5)

The hole milling process under both FIB conditions is effective at deterministic patterning of localized photoluminescence (PL). By spatially mapping the PL of milled

regions of the hBN flakes using a home-built confocal microscope, we find that FIB milling in Regions 1 and 2 both result in arrays of bright, highly visible spots with a periodicity matching that of the patterned features (see Figure 4.2(a),(d)). The contrast between the bright spots and the surrounding region between the bright spots is high ($> 20:1$). These surrounding regions have a PL ~ 5 -10 times lower than that regions of unmilled CVD hBN far from the milled sites (Figure 4.7(b)), which also have many randomly scattered sites of localized PL. The relatively low background near the patterned bright spots may be due to the long Gaussian tails of the FIB spot exposing areas near milled holes to a low ion dose, which is known to remove fluorescent organic surface residues and photoactive defects.⁶² Thus, it appears that the reduction of background PL is a convenient side-effect of the milling process. We note that, although FIB patterning clearly generates patterned PL, it is unknown if PL sources are localized inside the etched holes, on the hole edges, or in the unmilled regions between the edges. Techniques such as scanning near-field optical microscopy (SNOM), which overlay optical and topographical images, may help resolve this question. When we applied the conditions used in Regions 1 and 2 to wrinkled regions of CVD hBN and exfoliated hBN, we observed extremely low pattern visibility and we were unable to resolve single QEs. We suspect that the failure of our technique in wrinkled regions may be related to high compressive strain indicated by the wrinkles, while the failure in exfoliated hBN may be due to the high native defect density of the sample. (See the SI for optical data, AFM images, and further discussion of these regions (Figure 4.6, Figure 4.8)). Altogether, the flat regions of CVD hBN milled under either FIB condition generate spatially localized, high-contrast PL emission sites.

To assess the single-photon purity of individual bright spots formed by FIB milling, we perform antibunching measurements (see section 4.4 for details) and obtain second-degree correlation function data ($g^2(t)$), as seen in Figure 4.1(b). The antibunching data is fit by a three-level model to determine the antibunching depth of each milled site, as well as other photo-physical properties of the emitters (see section 4.4). The average number of photons was determined from $g^2(0)$ from the equation $g^2(0) = 1 - \frac{1}{n}$, where n is the average

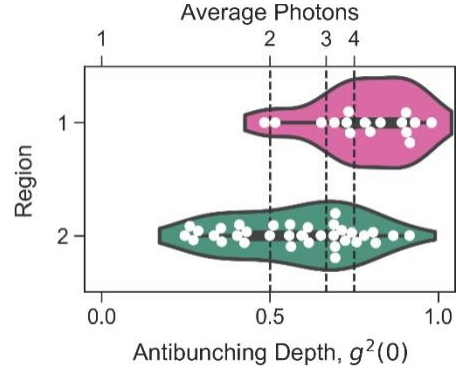


Figure 4.3: Distributions of degree of antibunching for both regions of FIB-treated CVD hBN (Region 2). Violin plot of antibunching depth for each region showing the larger overall degree of antibunching in region 2. Top axis labels show average photon numbers corresponding to antibunching

number of photons emitted.¹⁹ A site was denoted as zero average photon number if there was no PL signal from the site. All antibunching data is summarized in Figure 4.3, showing lines at antibunching values corresponding to 2, 3, and 4 average photons. The cutoffs correspond to the number of QEs for ideal single photon emission, which would have zero probability of two photon emission and no background light. Even without ideal single QEs, a $g^2(0) < 0.5$ indicates a single QE. We use this cutoff to classify sites as hosting single QEs, and do not attempt to perform any background subtraction. This is primarily because any significant background must be local, as indicated by the high contrast confocal image, and is further motivated by the inherent difficulty of accurately deconvolving background and signal light.

The FIB milling approach is effective at fabricating patterned single QEs. To assess the antibunching of milled regions and the effectiveness of making single QEs, we

characterized rows that appeared representative and characterized all FIB milled sites in those rows. In Region 1 we performed antibunching characterization on two adjacent rows of 9 sites. In Region 2 we characterized four rows of 9 sites; we also chose three adjacent rows as well as one row 20 μm above those three to check that the results were roughly consistent across the region. In Region 1, we measured an average antibunching depth of $g^2(0) = 0.78 \pm 0.15$, corresponding to an average photon number of 4.5. In this region, we found only one site exhibiting the antibunching signature of a single QE ($g^2(0) < 0.5$) out of 18 measured FIB milled holes, although all 16 that showed PL exhibited some amount of antibunching and 13 had antibunching characteristic of < 4 QEs. On the other hand, in Region 2, we measured an average antibunching depth of $g^2(0) = 0.57 \pm 0.19$, corresponding to an average photon number of 2.3. In this region, 11 out of 36 of milled holes had the antibunching characteristic of a single QE, demonstrating a single QE creation yield of 31%. Moreover, of the 34 of 36 holes in Region 2 that showed PL, all exhibited some amount of antibunching, demonstrating a QE creation yield of 94%. Our 31% yield of sites with single QEs is close to the theoretical maximum of 36.8% for a Poissonian QE creation process. The single QE yield is ~ 2.5 times greater than the yield achieved by nanopillar strain engineering.⁶³

Combining the site areal density (1 site per 1 μm^2) with the single QE yield, we calculate a single QE areal density of ~ 1 per 3 μm^2 . For a typical size hBN sheet ($\sim 50 \mu\text{m} \times 50 \mu\text{m}$), this density would create over 800 individually addressable single QEs. In order to estimate the amount of FIB milled edge necessary to create single QEs using our processing parameters, we use the hole circumference ($\sim 1.5 \mu\text{m}$) and the single QEs yield (~ 1 per 3 holes) to find a single QE linear density of ~ 1 per 5 μm of ion-milled edge.

In addition to exhibiting markedly different yield of single QE, Regions 1 and 2 also differ in their PL spectra. Typical spectra for sites in Region 1 ($g^2(0) > 0.5$) and Region 2 ($g^2(0) < 0.5$) are shown in Figure 4.2(c) and Figure 4.2(f), respectively (see section 4.4 for measurement details). The sharp peak at 2.27 eV corresponds to the silicon Raman peak for 532 nm excitation. Spectra from Region 1 tend to exhibit a single sharp emission line, but often have a broad background. Combined with the high pattern contrast in confocal images for this region, this suggests that the milling parameters in Region 1 create a large amount of background PL localized to the milling site. This background is at least one of the factors contributing to the low photon purity in this region. However, it is possible that there are multiple QEs contributing to a single sharp emission line. The very low amount of antibunching measured in Region 1 suggests that both factors likely contribute. In Region 2, we again often see a single primary emission line but the background is considerably lower compared to Region 1. Therefore, the higher energy and larger dose used to mill Region 2 is likely more effective at removing fluorescent contaminants and defects, and thereby leads to a lower background PL and a higher photon purity. Combined with the demonstrated high amount of antibunching in Region 2, this data shows that the high energy, high dose FIB parameters are preferred for QE creation.

Another key difference between Region 1 and 2 is the surface topography near the emission sites. Using AFM to measure the topography (see section 4.4), we find that the holes in Region 1 (low energy, low dose) are poorly-defined, non-uniform, and rough (see Figure 4.2b) with an arithmetic mean roughness, R_a , of 0.6 nm in the center of the hole. In contrast, the holes in Region 2 (high energy, high dose) have a well-defined

circular shape and a smooth profile (Figure 4.2(e)) with a depth ~ 5 nm over a lateral distance of 200 nm, and an arithmetic mean roughness, R_a , of 0.23 nm in the center of the hole. The roughness seen in Region 1 provides further evidence that fluorescing contaminants may not be thoroughly etched away under these FIB milling conditions. Through the formation of many deep pits, the milling in Region 1 created a large amount of in-plane edges on which QEs could form, in agreement with the hypothesis that edges are responsible for QE formation in hBN. Our AFM measurements suggest that a smooth, uniformly milled hole is optimal for single QE formation.

As compared to other techniques to activate QEs in hBN, the QEs created through FIB milling were similar in terms of the distribution of zero phonon lines (ZPLs), PL intensity, and optical stability. The distribution of ZPLs of these QEs, shown in Figure 4.4, was very similar to QEs found in CVD hBN suspended on nanopillars.⁶³ In the setup we used to take antibunching measurements we used a filter light with energy above 2.25 eV, however the phonon sideband from those emitters was below the cutoff and allowed through to our detectors. In PL spectra, we find phonon sidebands at 150 ± 23 meV from their respective zero phonon lines, consistent with previous observations.^{28,30,31,35,61} To further compare our QEs to those created by other methods, we measure PL intensity vs. power for our emitters in Region 2 and fit that data to a first-order saturation model,³⁷ $I(P) = I_\infty P / (P + P_{sat})$ (see Figure 4.7c). We find that our brightest emitter has an I_∞ of

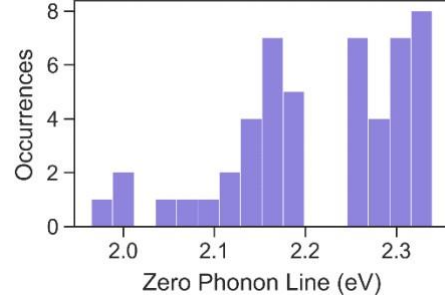


Figure 4.4: Zero phonon line energies across all emitters for which there was a clearly identifiable central emission line showing a similar distribution of energies compared to previous observations of hBN quantum emitters.

roughly 2.6 Mcps, on par with other hBN quantum emitters.^{28,30,31,35,61} Across the 11 single QEs, roughly 33% were optically stable for the entire measurement duration – a few hours of illumination at 80 μ W excitation power. Of these 11, only one bleached entirely and stopped emitting PL. The remaining six exhibited some blinking without fully bleaching. This blinking and bleaching behavior is similar to what is observed in hBN QEs^{32,65} created using other methods, suggesting that our FIB milling procedure is at least as effective for creating optically-stable emitters.

The FIB milling approach produces a high density of individually addressable single QEs. Leveraging our ability to generate large

quantities of single QEs, we study the PL blinking dynamics of large numbers of hBN QEs in a relatively uniform surrounding environment (*e.g.* substrate, charge, strain). We measure the probability distribution of PL intensity for 10 single QEs as histograms binned by brightness at fixed 80 μ W excitation laser power (Fig. 4.5(a)). See section 4.5 for PL intensity versus time. While some QEs show a single peak (QE 1 to 6), others (QE7-10) show two peaks, suggesting a bright and dim state. Furthermore, some have a

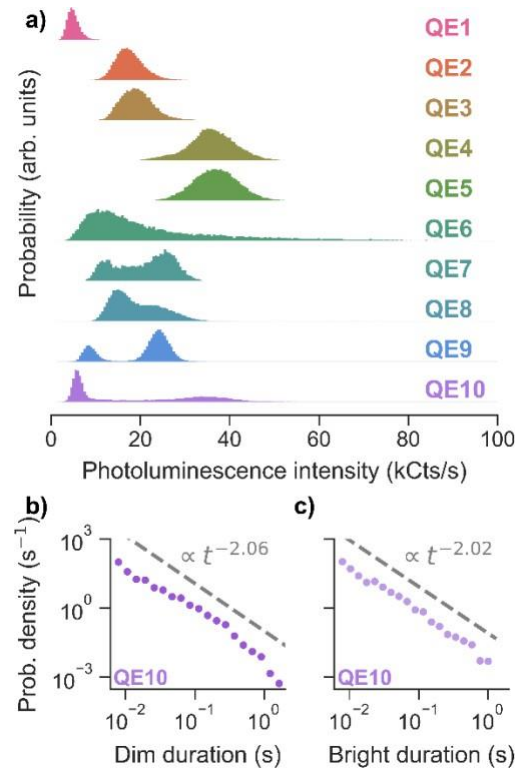


Figure 4.5: (a) PL intensity of the single QEs. The last one, labeled QE10, shows blinking behavior that we analyze in b and c. (b) Probability density of the dim state lifetime. The offset dashed grey line is a power law fit to the data with power 2.06 ± 0.08 . (c) Probability density of the bright state lifetime. The offset dashed grey line is a power law fit to the data with power 2.02 ± 0.05 .

narrow distribution centered near a single intensity, while others are broader and even exhibit long tails. To characterize the blinking behavior of a single QE with distinct bright (or “on”) and dim (or “off”) states – that is, a QE that exhibits PL distributions with two non-overlapping peaks in Fig 4.5a – we measure the probability that a given blink will last a certain duration of time. Performing this analysis on Q10, we specify the dim state as PL intensity < 17 kCounts/s and the bright state as PL intensity > 19 kCounts/s for QE10 at this excitation power. This type of analysis is only appropriate for two-state emitters with a clear threshold (*e.g.* QE9 and 10). The probability density data for the dim (Figure 4.5(b)) and bright (Figure 4.5(c)) states show that short blinks occur more often than long-lasting blinks. We fit these data to a dominant power law, probability $\propto t^{-2}$ for QE10 over the timescales shown, where t is the state duration, consistent with the power law observed in other quantum emitters,^{66–70} and in contrast to systems that show an exponential behavior with a single characteristic time.^{71–74} The dominant power law we observe rules out a simple charging model⁷⁵, which would predict an exponential distribution, but leaves a variety of blinking models as possibilities,⁷⁴ including modified charging models, where the barrier between two states can vary⁷⁶. The bright state of QE9 does not show a simple power law fit over the same time scale (see section 4.7). It may be possible to mitigate PL intensity fluctuation through the use of a passivating layer,³² or a more pristine substrate.⁶⁵ However, this analysis, together with the ability to generate many single QEs, may help to shed light on the mechanisms governing PL instabilities in hBN QEs by showing that something other than simple charging is causing this blinking.

While we have found a combination of dose, energy, and defocus which yields high quality QEs, it may be possible to push the single photon purity and density of these QEs higher through further exploration of the rich parameter space available with FIB milling. Beyond the simple parameters we explored, changing FIB defocus or angle may reduce roughness of milled hBN^{77,78} and result in a reduced background PL. Due to the relative independence of QE formation to ion type,³⁵ a helium FIB or electron beam could be used to perform this milling in a less destructive way^{79–81} and enable greater single photon purity. Our approach achieved a single QE density of $0.33/\mu\text{m}^2$, which is largely determined by the hole array density ($1/\mu\text{m}^2$). Thus, a simple way to increase the single QE density may be to decrease the hole spacing, perhaps while altering hole geometry to maintain a constant perimeter. It should also be possible to expand this technique beyond electron or ion beam milling by using a combination of photolithography and reactive ion etch (RIE) processes⁸² to pattern holes in hBN. Such a generalization of this technique would dramatically lower the barrier for further studies and applications of hBN QEs.

The formation process of these QEs is difficult to ascertain because the defect structure is still poorly understood.⁸³ However, our AFM measurements show that the FIB process does not result in high curvature, suggesting that the process of QE formation via edge creation is distinct from the high curvature method previously demonstrated.⁶³ The dual QE generation pathways (*i.e.* edges or high curvature) may be due to local band structure shifts due to strain⁸⁴ or edge relaxation.^{85,86} It may also be that high strain or edges allow for local reconstruction of the hBN,^{87,88} leading to formation of optically-active Stone-Wales-like defects. A future study correlating high resolution optical images with

topographical images (*i.e.* using SNOM or colocalized optical/AFM) could provide valuable insight into the nature of QE formation in hBN.

4.3. Conclusion

In this work, we have used FIB milling to generate patterned single QEs in hBN with a yield of 31%. Our FIB-based fabrication method fills in the crucial need to create and control the location of single QEs in hBN, thus enabling the integration of these QEs into chip-scale plasmonic, photonic, and optomechanical devices for quantum information applications in ambient conditions. Our technique will provide large numbers of individually addressable single hBN QEs for QE-based sensing applications,⁸⁹ and significantly lowers the barrier for studying the physics of hBN QEs and allows for more expansive surveys of their properties.

4.4. Methods and Materials

Sample fabrication and surface characterization

The samples used in this study were prepared by polymer transfer⁹⁰ of ~15 layer CVD hBN purchased from Graphene Supermarket. Samples were annealed in oxygen at 850C for a half hour both before and after focused ion beam milling in order to remove hydrocarbon contaminants. Focused ion beam milling was performed on a FEI Helios Dual-Beam gallium FIB with beam parameters set as noted above. Before milling, the sample and chamber were plasma cleaned with air for five minutes to remove residual hydrocarbons. AFM measurements were performed on a Bruker Dimension FastScan Atomic Force Microscope operated in PeakForce mode.

Optical measurements

We performed initial confocal scans and antibunching experiments of QEs in a home-built confocal microscope equipped with a 532 nm solid state laser (OptoEngine), 100x 0.7 NA objective and two avalanche photodiodes (Micro Photon Devices) in a Hanbury Brown-Twiss setup. All optical measurements were performed at an excitation power of roughly 80 μ W. Time-correlated single photon counting was performed on a PicoQuant TimeHarp 260. These measurements were used to determine if PL sources were QEs, and also yielded their average photon number, non-radiative and radiative lifetimes, and bunching amplitude. These parameters were extracted from antibunching measurements by fitting our data to a simple model¹⁹ for a three-level system: $g^2(t) = 1 - \rho^2 + \rho^2[1 - (1 - a)e^{-\frac{|t|}{\tau_1} + ae^{-\frac{|t|}{\tau_2}}}]$, where a is the bunching amplitude, τ_1 is the non-radiative lifetime, τ_2 is the radiative lifetime, and $\rho^2 = 1 - g^2(0)$ where $g^2(0)$ is the degree of antibunching. Photon number in a given milled hole was determined by binning $g^2(0)$ values according to $g^2(0) = 1 - \frac{1}{n}$. We measured the spectra of QEs using a commercial Witec Raman spectrometer equipped with a Peltier-cooled Andor iDus CCD.

4.5. Supplementary Information

Focused ion beam milling of wrinkled hBN grown by chemical vapor deposition

Processing of wrinkled chemical vapor deposition-grown (CVD) hexagonal boron nitride (hBN) gave a very poor yield of QEs (Figure 4.6) despite using intermediate parameters

to those which gave many QEs. We suspect that the QEs may have difficulty forming because these wrinkles indicate that the polymer transfer process damaged the hBN or that the hBN is under large compressive strain.

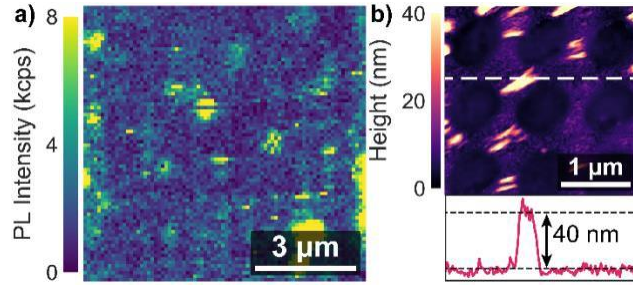


Figure 4.6: (a) Confocal image of a region (milled at high energy, low dose) of CVD hBN showing very poor visibility of the array (b) AFM image of the same region showing the large amount of wrinkles.

Further atomic force microscope characterization of hBN

Atomic force microscopy (AFM) on the CVD hBN material shows that the surface is fairly rough and textured (Figure 4.7(a)). This native texture of the hBN may have contributed to the high yield of QEs that we were able to achieve with our FIB and anneal procedure. On the other hand, AFM measurements on exfoliated hBN (Figure 4.8(b)) show that the surface is very smooth. This suggests that a good surface quality may not be sufficient indication of material quality for hBN QE formation.

Confocal microscopy on unmilled CVD hBN

To more completely understand how the CVD hBN was different from the exfoliated hBN, we performed confocal microscopy on unmilled regions of our CVD hBN nearby regions that had been milled and thoroughly characterized. These images show many areas of highly localized PL, which may suggest that this CVD hBN hosts a high number of QEs with only annealing.

Measurement of saturation photoluminescence intensity

To determine the efficiency and brightness of the QEs created using our FIB milling technique, we measure the PL intensity at various powers and fit the data to a first-order

saturation model of the form $I(P)=I_{\infty} P/(P+P_{\text{sat}})$, as noted in the main text. Figure S(c) shows PL intensity vs. excitation power data and corresponding fit for the brightest emitter found in region 2 (high dose, high energy FIB milled CVD hBN). Calculated I_{∞} for this QE was 2.6 Megacounts per second.

Example of spectra with zero phonon lines near 532 nm

Some spectra of quantum emitters (QEs) we found exhibited zero phonon lines with high energy, very close to

the excitation energy. We had an optical filter in our confocal microscope that removed high energy zero phonon lines, but we measured the antibunching for these QEs and found that they were quantum emitters. Figure 4.7(d) shows an example of one such high energy zero phonon line.

Quantum emitter creation in exfoliated hBN

Attempts to create QEs in exfoliated hBN (HQGraphene) were successful in creating some QEs, but FIBed areas always had a broad background. This was the case using the same procedure as with CVD hBN, as well as with modified anneals and FIBing procedures. We found in general that we had poor QE visibility. We attribute this

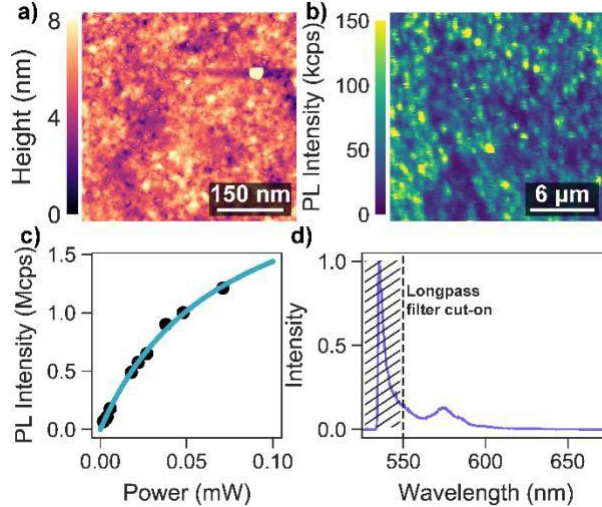


Figure 4.7: (a) Atomic force microscope image of a region of CVD hBN nearby the FIBed regions characterized. (b) Confocal microscope image of unmilled hBN showing a large amount of localized PL. (c) Plot of photoluminescence intensity vs. excitation power showing a best fit to a linear saturation model. (d) Spectrum of a low wavelength emitter showing the PL collected and spectrum observed with a 550 nm long pass filter.

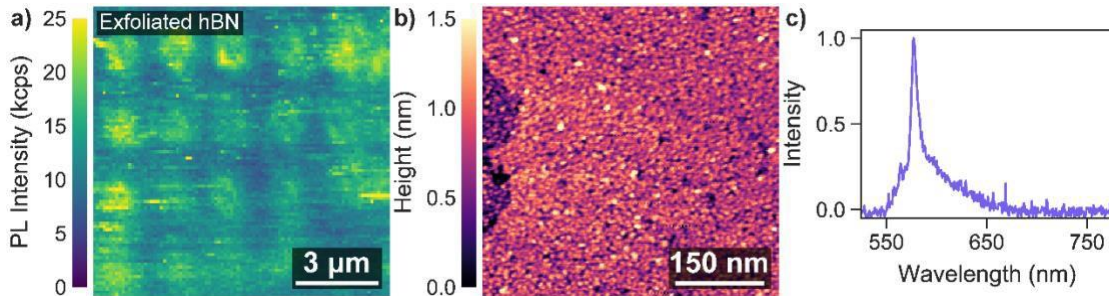


Figure 4.8: (a) Confocal image of a FIBed region of exfoliated hBN showing the poor pattern visibility. (b) Atomic force microscope image of a region of unirradiated exfoliated hBN after processing. Surface roughness is much less than the CVD hBN. (c) Example of the best spectrum found on a FIBed exfoliated flake. Sharp peak may indicate a QE, but broad background prevents strong antibunching.

to a large amount of background PL, likely due to a large amount of native defects. After extended annealing (3 hours at 500C) we were able activate some QEs with sharp emission lines, see Figure 4.7(c). However, we were unable to affect the broad background with any amount of annealing.

Photoluminescence trajectories

The photoluminescence trajectories for each of the 11 quantum emitters is shown in Figure 4.9 All QEs were excited with the same cw laser power, 80 μW, measured at the back opening of the objective. We maximized the polarization angle of the excitation laser prior to measuring the PL intensity of each QE. The collection rate was either 100 Hz or 125 Hz, corresponding to time bin widths of 10 ms or 8 ms, as follows: QE1 at 125 Hz, QE2 at 100Hz, QE3 at 100Hz, QE4 at 125 Hz, QE5 at 125 Hz, QE6 at 100 Hz, QE7 at 100Hz, QE8 at 100Hz, QE9 at 125 Hz, and QE10 at 125 Hz.

Power dependence of bright and dim state

Although the dim state emits fewer photons per second than the bright state, it is not fully ‘off.’ The dim state increases in PL intensity as the excitation laser power

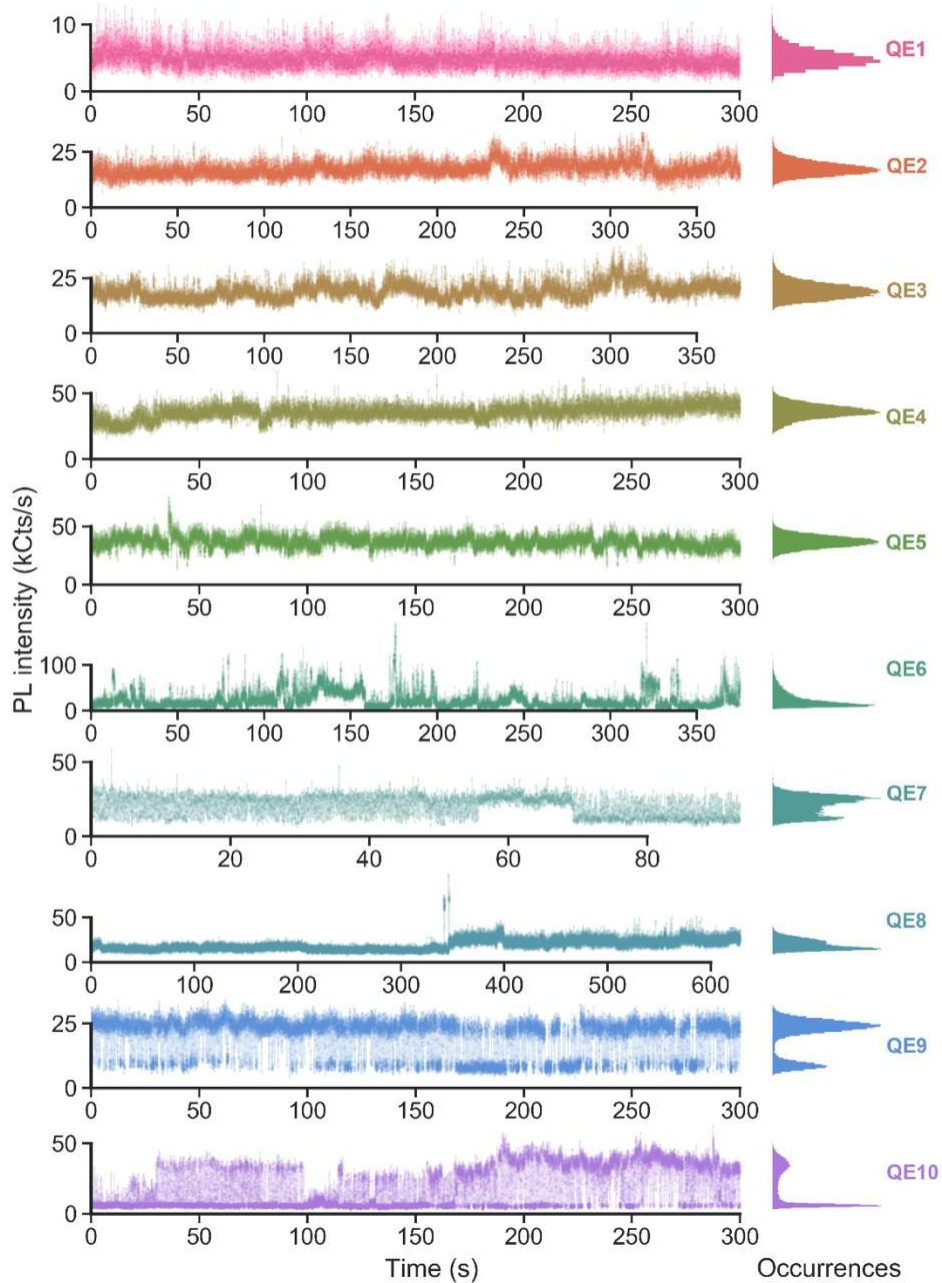
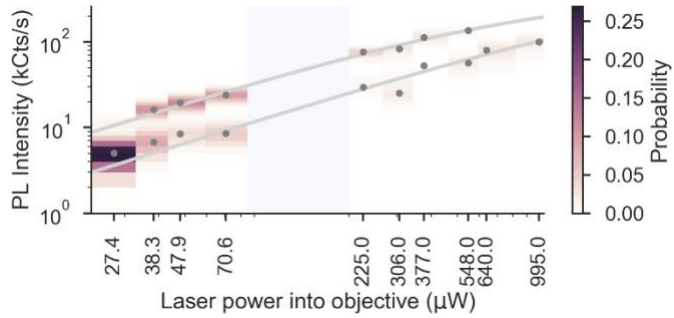


Figure 4.9: Photoluminescence trajectories. **Left:** Photoluminescence (PL) intensity versus time for QE1 to 10. **Right:** Histograms corresponding to each trajectory. The histograms are the same as Fig 4.3a in section 4.3.

increases, as shown in Figure 4.10 with fit to the first-order saturation model, similar to Figure 4.7(c).

A long-duration state does not predict another

We observe from the Fig 4.9 histogram that QE9 has two distinct PL intensity levels, and, as was done for QE10 in section 4.3 (Fig. 4.4b,c), we calculate the



probability density for the duration of the dim state and the bright state

Figure 4.10: The bright state and dim state of QE9 both show an increase in PL intensity as the excitation laser power is increased.

(Fig 4.11), where we define the bright state as having PL intensity > 16.1 kCts/s and the dim state as having PL intensity < 14.1 kCts/s for QE9 at this laser excitation power. This threshold is chosen based on the minimum of the histogram shown in Fig. 4.9. To investigate whether a long lasting bright state is expected to be followed by a second-long lasting bright state, we

plot each state duration as a function of the previous state duration in Fig. 4.11. There is no clear trend for bright or dim states, suggesting a lack of correlation between the previous state duration and the current state duration.

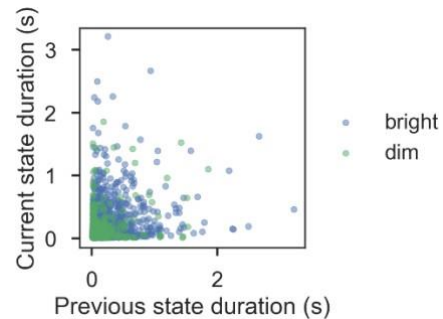


Figure 4.11: There is no clear trend between each bright state duration and the previous bright state duration (blue) nor between each dim state duration and the previous dim state duration (green) in the PL trajectory of QE9.

Limitations of the dominant power law

It is a mathematical impossibility for a probability distribution function (PDF) to show a power law that persists to infinity, because the integral would not converge, so the total

probability would be infinite. Therefore, there must be a duration above which we observe a cut-off to the power law trend. Here we discuss evidence for such a cut-off in the two-state blinking data. For Figure 4.4b,c in section 4.3 and Fig 4.9 here, the duration is first binned in unequal but logarithmically evenly spaced duration

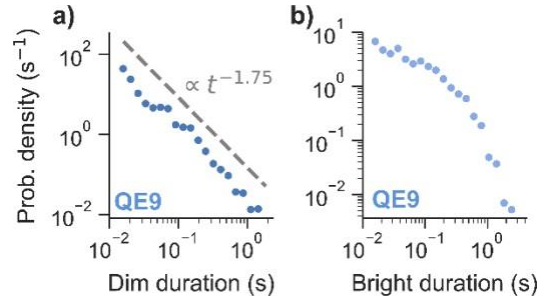


Figure 4.12: Probability density of duration of each state for QE9. The dim state (a) shows a dominant power law with slope $\alpha = 1.75 \pm 0.06$, while the bright state (b) deviates from power law behavior.

bin widths⁹¹, then the probability is normalized by the duration bin width to obtain the probability density in units of inverse seconds. We observe that the dim state duration for QE9 shows a dominant power law, while the bright state duration deviates from power law behavior. The shape of the data trend suggests a truncated power law, and we argue that, in fact, the probability distribution of the dim duration of QE9 and the probability distribution for both the bright and dim durations of QE10 are each best fit by a truncated power law, though it is not evident from the visible trend of the probability distribution function in Fig. 4.12(a). We need to consider the cumulative distribution function for more insight.

The complementary cumulative distribution function (1-CDF) is the integral over the probability distribution function $p(t')$ from a given state duration t up to positive infinity,

$$P(t) = \int_t^{\infty} p(t') dt'.$$

Therefore, the shortest duration on a 1-CDF plot always represents 100% of the data. The complementary CDF is calculated by counting the fraction of blinking events

that are longer than a given duration t . The number of data points is therefore given by the number of blink events and the horizontal axis on the 1-CDF plot is *not* collected into bins. The probability distribution is the derivative of the 1-CDF and we must choose appropriate bins for it, as discussed above, in contrast to the 1-CDF.

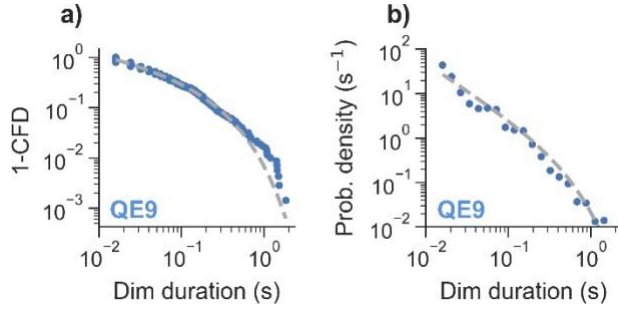


Figure 4.13: Truncated power law fit of dim state of QE9. The fit to the complementary cumulative distribution function (1-CDF, a) provides fitting parameters for the probability distribution function (PDF, b) to fit to a truncated power law.

If the probability distribution function (PDF) is a power law,

$$p_{\text{pow}}(t) = Ct^{-\alpha},$$

where C and α are constants, then by integrating we observe that the complementary CDF $P_{\text{pow}}(t)$ must also be a power law,

$$P_{\text{pow}}(t) = \frac{C}{\alpha - 1} t^{-(\alpha-1)}.$$

On a log-log plot, this will appear as a straight line with slope $1 - \alpha$. The data for QE9 and QE10, however, consistently show a nonlinear curve for the complementary CDF (Fig 4.13(a)), indicating that there are limitations to the power law model for these probability curves.

To better fit the data, we may, instead, model the probability distribution as a truncated power law. This is consistent with the behavior of intermittent fluorescence of quantum emitters in other systems, particularly blinking quantum dots^{74,92–95}. We now model the PDF as a truncated power law,

$$p(t) = Ct^{-\alpha} \exp\left(-\frac{t}{t_c}\right),$$

where t_c is the cut-off duration time. Compared to a power law, this curve fit better matches the data trend observed in Fig. 4.12(b) and 4.13(a). By integrating, we find the complementary CDF must then be given by

$$P(t) = Ct_c^{1-\alpha} \Gamma\left(1 - \alpha, \frac{t}{t_c}\right),$$

where Γ is the *incomplete gamma* function. This function is fit to the 1-CDF curves in Fig. 4.13(a) with three fitting parameters: the coefficient C , the exponent α , and the cut-off time t_c . By fitting to the 1-CDF instead of the PDF, we avoid artifacts that may arise from the choice of time duration bin size, which may occur for fits of the PDF, though the choice of threshold between bright and dim states may still affect the fitting parameters⁹³. The fit gives $\alpha = 1.22 \pm 0.02$ and $t_c = 0.47 \pm 0.03$ s. These same fitting parameters are then used to calculate the curve shown on the probability curves in Fig. 4.13(b). While both a power law fit and a truncated power law fit are plausible models for the PDF, only the truncated power law is plausible as a fit for the 1-CDF.

CHAPTER V

CONCLUDING REMARKS

With the studies described in the preceding two chapters, I have worked to increase the usefulness and potential for integration of hBN single photon emitters. In chapter III, I described work performed characterizing single photon emitters found in boron nitride nanococoons. The primary useful feature that I identified with this zero dimensional allotrope of boron nitride was reduction of the wavelength variation of hosted single photon emitters by a factor of 5 compared to 2D hBN flakes. We suspect that this reduced wavelength variation was due to their increased structural robustness compared to a thin, flat 2D flake. The spectral features combined with their nanoscale size, suggest that single photon emitters hosted by boron nitride nanococoons possess a high potential for incorporation into photonic structures such as waveguides or photonic crystal cavities with a pick-and-place strategy. In chapter IV, I described a technique that I developed for controlled creation of single photon emitters in hexagonal boron nitride. This technique is only the second demonstration of controlled single photon emitter creation in this material¹³ and, crucially, is material and substrate agnostic. Our technique thus possesses a greatly expanded range of integration strategies where it could be applied. Specifically, our technique will likely prove to be highly useful for large-scale integration of hBN emitters into arrays of photonic/plasmonic or other optoelectomechanical devices.

Together, the two studies that I have described in this dissertation serve to advance the technological usefulness of single photon emitters in hexagonal boron nitride. Combining these techniques with recent demonstrated techniques for further control of the wavelength variation using either Stark⁹⁶ or strain tuning⁹ will enable easy integration of hexagonal boron nitride with photonic devices. Furthermore, the narrow linewidth at room temperature that has been found in some hexagonal boron nitride single photon emitters⁹⁷ combined with techniques for stabilization of emitters against spectral diffusion⁶⁵ may soon enable on-chip indistinguishable single photons for demonstration of quantum information technologies.

REFERENCES CITED

- (1) Shor, P. W. Algorithms for Quantum Computation: Discrete Logarithms and Factoring. In *Proceedings 35th Annual Symposium on Foundations of Computer Science*; 1994; pp 124–134. <https://doi.org/10.1109/SFCS.1994.365700>.
- (2) Childs, A. M.; Maslov, D.; Nam, Y.; Ross, N. J.; Su, Y. Toward the First Quantum Simulation with Quantum Speedup. *PNAS* **2018**, *115* (38), 9456–9461. <https://doi.org/10.1073/pnas.1801723115>.
- (3) Bennett, C. H.; Brassard, G.; Salvail, L.; Smolin, J. Experimental Quantum Cryptography. *J. Cryptology* **1992**, *5* (1), 3–28. <https://doi.org/10.1007/BF00191318>.
- (4) Yimsiriwattana, A.; Jr, S. J. L. Distributed Quantum Computing: A Distributed Shor Algorithm. In *Quantum Information and Computation II*; International Society for Optics and Photonics, 2004; Vol. 5436, pp 360–372. <https://doi.org/10.1117/12.546504>.
- (5) Aaronson, S.; Arkhipov, A. The Computational Complexity of Linear Optics. *Theory of Computing* **2013**, *9* (1), 143–252. <https://doi.org/10.4086/toc.2013.v009a004>.
- (6) Knill, E.; Laflamme, R.; Milburn, G. J. A Scheme for Efficient Quantum Computation with Linear Optics. *Nature* **2001**, *409* (6816), 46–52. <https://doi.org/10.1038/35051009>.
- (7) Jungwirth, N. R.; Calderon, B.; Ji, Y.; Spencer, M. G.; Flatté, M. E.; Fuchs, G. D. Temperature Dependence of Wavelength Selectable Zero-Phonon Emission from Single Defects in Hexagonal Boron Nitride. *Nano Lett.* **2016**, *16* (10), 6052–6057. <https://doi.org/10.1021/acs.nanolett.6b01987>.
- (8) Grosso, G.; Moon, H.; Lienhard, B.; Ali, S.; Efetov, D. K.; Furchi, M. M.; Jarillo-Herrero, P.; Ford, M. J.; Aharonovich, I.; Englund, D. Tunable and High-Purity Room Temperature Single-Photon Emission from Atomic Defects in Hexagonal Boron Nitride. *Nat Commun* **2017**, *8* (1), 1–8. <https://doi.org/10.1038/s41467-017-00810-2>.
- (9) Mendelson, N.; Doherty, M.; Toth, M.; Aharonovich, I.; Tran, T. T. Strain Engineering of Quantum Emitters in Hexagonal Boron Nitride. *arXiv:1911.08072 [cond-mat, physics:physics]* **2020**.
- (10) Martínez, L. J.; Peline, T.; Waselowski, V.; Maze, J. R.; Gil, B.; Cassabois, G.; Jacques, V. Efficient Single Photon Emission from a High-Purity Hexagonal Boron Nitride Crystal. *Phys. Rev. B* **2016**, *94* (12), 121405. <https://doi.org/10.1103/PhysRevB.94.121405>.

- (11) Ziegler, J.; Blaikie, A.; Fathalizadeh, A.; Miller, D.; Yasin, F. S.; Williams, K.; Mohrhardt, J.; McMorrán, B. J.; Zettl, A.; Alemán, B. Single-Photon Emitters in Boron Nitride Nanococoons. *Nano Lett.* **2018**, *18* (4), 2683–2688. <https://doi.org/10.1021/acs.nanolett.8b00632>.
- (12) Choi, S.; Tran, T. T.; Elbadawi, C.; Lobo, C.; Wang, X.; Juodkazis, S.; Seniutinas, G.; Toth, M.; Aharonovich, I. Engineering and Localization of Quantum Emitters in Large Hexagonal Boron Nitride Layers. *ACS Appl. Mater. Interfaces* **2016**, *8* (43), 29642–29648. <https://doi.org/10.1021/acsami.6b09875>.
- (13) Proscia, N. V.; Shotan, Z.; Jayakumar, H.; Reddy, P.; Dollar, M.; Alkauskas, A.; Doherty, M.; Meriles, C. A.; Menon, V. M. Near-Deterministic Activation of Room Temperature Quantum Emitters in Hexagonal Boron Nitride. *Optica* **2018**, *5*, 1128.
- (14) Ziegler, J.; Klaiss, R.; Blaikie, A.; Miller, D.; Horowitz, V. R.; Alemán, B. J. Deterministic Quantum Emitter Formation in Hexagonal Boron Nitride via Controlled Edge Creation. *Nano Lett.* **2019**, *19* (3), 2121–2127. <https://doi.org/10.1021/acs.nanolett.9b00357>.
- (15) Glauber, R. J. The Quantum Theory of Optical Coherence. *Phys. Rev.* **1963**, *130* (6), 2529–2539. <https://doi.org/10.1103/PhysRev.130.2529>.
- (16) Kimble, H. J.; Dagenais, M.; Mandel, L. Photon Antibunching in Resonance Fluorescence. *Phys. Rev. Lett.* **1977**, *39* (11), 691–695. <https://doi.org/10.1103/PhysRevLett.39.691>.
- (17) Stoler, D. Photon Antibunching and Possible Ways to Observe It. *Phys. Rev. Lett.* **1974**, *33* (23), 1397–1400. <https://doi.org/10.1103/PhysRevLett.33.1397>.
- (18) Chandra, N.; Prakash, H. Anticorrelation in Two-Photon Attenuated Laser Beam. *Phys. Rev. A* **1970**, *1* (6), 1696–1698. <https://doi.org/10.1103/PhysRevA.1.1696>.
- (19) Brouri, R.; Beveratos, A.; Poizat, J. P.; Grangier, P. Photon Antibunching in the Fluorescence of Individual Color Centers in Diamond. *Optics letters* **2000**, *25* (17), 1294–1296. <https://doi.org/10.1364/OL.25.001294>.
- (20) Pellizzari, T.; Ritsch, H. Photon Statistics of the Three-Level One-Atom Laser. *Journal of Modern Optics* **2007**. <https://doi.org/10.1080/09500349414550601>.
- (21) Jungwirth, N. R. AN EXPLORATION OF DEFECT-BASED SINGLE PHOTON SOURCES: ZINC OXIDE AND HEXAGONAL BORON NITRIDE. **2018**. <https://doi.org/10.7298/8set-yf08>.

- (22) Toyli, D. M.; de las Casas, C. F.; Christle, D. J.; Dobrovitski, V. V.; Awschalom, D. D. Fluorescence Thermometry Enhanced by the Quantum Coherence of Single Spins in Diamond. *Proceedings of the National Academy of Sciences* **2013**, *110* (21), 8417–8421. <https://doi.org/10.1073/pnas.1306825110>.
- (23) Kucsko, G.; Maurer, P. C.; Yao, N. Y.; Kubo, M.; Noh, H. J.; Lo, P. K.; Park, H.; Lukin, M. D. Nanometre-Scale Thermometry in a Living Cell. *Nature* **2013**, *500* (7460), 54–58. <https://doi.org/10.1038/nature12373>.
- (24) Mohan, N.; Chen, C. S.; Hsieh, H. H.; Wu, Y. C.; Chang, H. C. In Vivo Imaging and Toxicity Assessments of Fluorescent Nanodiamonds in *Caenorhabditis Elegans*. *Nano Letters* **2010**, *10* (9), 3692–3699. <https://doi.org/10.1021/nl1021909>.
- (25) Lee, J. C.; Bracher, D. O.; Cui, S.; Ohno, K.; McLellan, C. A.; Zhang, X.; Andrich, P.; Alemán, B.; Russell, K. J.; Magyar, A. P.; Aharonovich, I.; Bleszynski Jayich, A.; Awschalom, D.; Hu, E. L. Deterministic Coupling of Delta-Doped Nitrogen Vacancy Centers to a Nanobeam Photonic Crystal Cavity. *Applied Physics Letters* **2014**, *105* (26), 1–4. <https://doi.org/10.1063/1.4904909>.
- (26) Pichler, H.; Choi, S.; Zoller, P.; Lukin, M. D. Universal Photonic Quantum Computation via Time-Delayed Feedback. *Proceedings of the National Academy of Sciences* **2017**, *114* (43), 11362–11367. <https://doi.org/10.1073/pnas.1711003114>.
- (27) Kalb, N.; Reiserer, A. A.; Humphreys, P. C.; Bakermans, J. J. W.; Kamerling, S. J.; Nickerson, N. H.; Benjamin, S. C.; Twitchen, D. J.; Markham, M.; Hanson, R. Entanglement Distillation between Solid-State Quantum Network Nodes. *Science* **2017**, *356* (6341), 928–932. <https://doi.org/10.1126/science.aan0070>.
- (28) Tran, T. T.; Bray, K.; Ford, M. J.; Toth, M.; Aharonovich, I. Quantum Emission From Hexagonal Boron Nitride Monolayers. *Nature Nanotechnology* **2015**, *11* (January), 37–42. <https://doi.org/10.1038/nnano.2015.242>.
- (29) Exarhos, A. L.; Hopper, D. A.; Grote, R. R.; Alkauskas, A.; Bassett, L. C. Optical Signatures of Quantum Emitters in Suspended Hexagonal Boron Nitride. *ACS Nano* **2017**, *11* (3), 3328–3336. <https://doi.org/10.1021/acsnano.7b00665>.
- (30) Tran, T. T.; Elbadawi, C.; Totonjian, D.; Lobo, C. J.; Grosso, G.; Moon, H.; Englund, D. R.; Ford, M. J.; Aharonovich, I.; Toth, M. Robust Multicolor Single Photon Emission from Point Defects in Hexagonal Boron Nitride. *ACS Nano* **2016**, *10* (8), 7331–7338. <https://doi.org/10.1021/acsnano.6b03602>.

- (31) Chejanovsky, N.; Rezai, M.; Paolucci, F.; Kim, Y.; Rendler, T.; Rouabeh, W.; Fávvaro De Oliveira, F.; Herlinger, P.; Denisenko, A.; Yang, S.; Gerhardt, I.; Finkler, A.; Smet, J. H.; Wrachtrup, J. Structural Attributes and Photodynamics of Visible Spectrum Quantum Emitters in Hexagonal Boron Nitride. *Nano Letters* **2016**, *16* (11), 7037–7045. <https://doi.org/10.1021/acs.nanolett.6b03268>.
- (32) Shotan, Z.; Jayakumar, H.; Considine, C. R.; Mackoite, M.; Fedder, H.; Wrachtrup, J.; Alkauskas, A.; Doherty, M. W.; Menon, V. M.; Meriles, C. A. Photoinduced Modification of Single-Photon Emitters in Hexagonal Boron Nitride. *ACS Photonics* **2016**, *3* (12), 2490–2496. <https://doi.org/10.1021/acsphotonics.6b00736>.
- (33) Grosso, G.; Moon, H.; Lienhard, B.; Ali, S.; Efetov, D. K.; Furchi, M. M.; Jarillo-Herrero, P.; Ford, M. J.; Aharonovich, I.; Englund, D. Tunable and High Purity Room-Temperature Single Photon Emission from Atomic Defects in Hexagonal Boron Nitride. *Nature Communications* **2016**, *8*, 1–8. https://doi.org/10.1364/CLEO_AT.2017.JM3E.5.
- (34) Jungwirth, N. R.; Calderon, B.; Ji, Y.; Spencer, M. G.; Flatté, M. E.; Fuchs, G. D. Temperature Dependence of Wavelength Selectable Zero-Phonon Emission from Single Defects in Hexagonal Boron Nitride. *Nano Letters* **2016**, *16* (10), 6052–6057. <https://doi.org/10.1021/acs.nanolett.6b01987>.
- (35) Choi, S.; Tran, T. T.; Elbadawi, C.; Lobo, C.; Wang, X.; Juodkazis, S.; Seniutinas, G.; Toth, M.; Aharonovich, I. Engineering and Localization of Quantum Emitters in Large Hexagonal Boron Nitride Layers. *ACS Applied Materials and Interfaces* **2016**, *8* (43), 29642–29648. <https://doi.org/10.1021/acsami.6b09875>.
- (36) Kianinia, M.; Regan, B.; Tawfik, S. A.; Tran, T. T.; Ford, M. J.; Aharonovich, I.; Toth, M. Robust Solid-State Quantum System Operating at 800 K. *ACS Photonics* **2017**, *4* (4), 768–773. <https://doi.org/10.1021/acsphotonics.7b00086>.
- (37) Martínez, L. J.; Peline, T.; Waselowski, V.; Maze, J. R.; Gil, B.; Cassabois, G.; Jacques, V. Efficient Single Photon Emission from a High-Purity Hexagonal Boron Nitride Crystal. *Physical Review B* **2016**, *94* (12), 1–5. <https://doi.org/10.1103/PhysRevB.94.121405>.
- (38) Georgakilas, V.; Perman, J. A.; Tucek, J.; Zboril, R. Broad Family of Carbon Nanoallotropes: Classification, Chemistry, and Applications of Fullerenes, Carbon Dots, Nanotubes, Graphene, Nanodiamonds, and Combined Superstructures. *Chemical Reviews* **2015**, *115* (11), 4744–4822. <https://doi.org/10.1021/cr500304f>.
- (39) Cohen, M. L.; Zettl, A. The Physics of Boron Nitride Nanotubes. *Physics Today* **2010**, *63* (11), 34–38. <https://doi.org/10.1063/1.3518210>.

- (40) Fathalizadeh, A.; Pham, T.; Mickelson, W.; Zettl, A. Scaled Synthesis of Boron Nitride Nanotubes, Nanoribbons, and Nanococoons Using Direct Feedstock Injection into an Extended-Pressure, Inductively-Coupled Thermal Plasma. *Nano Letters* **2014**, *14* (8), 4881–4886. <https://doi.org/10.1021/nl5022915>.
- (41) Seifert, G.; Fowler, P. W.; Mitchell, D.; Porezag, D.; Frauenheim, T. Boron-Nitrogen Analogues of the Fullerenes: Electronic and Structural Properties. *Chemical Physics Letters* **1997**, *268* (5–6), 352–358. [https://doi.org/10.1016/s0009-2614\(97\)00214-5](https://doi.org/10.1016/s0009-2614(97)00214-5).
- (42) Koponen, L.; Tunturivuori, L.; Puska, M. J.; Nieminen, R. M. Photoabsorption Spectra of Boron Nitride Fullerene-like Structures. *Journal of Chemical Physics* **2007**, *126* (21), 1–4. <https://doi.org/10.1063/1.2741524>.
- (43) Cumings, J.; Zettl, A. Mass-Production of Boron Nitride Double-Wall Nanotubes and Nanococoons. *Chemical Physics Letters* **2000**, *316* (3–4), 211–216. [https://doi.org/10.1016/S0009-2614\(99\)01277-4](https://doi.org/10.1016/S0009-2614(99)01277-4).
- (44) Tohei, T.; Kuwabara, A.; Oba, F.; Tanaka, I. Debye Temperature and Stiffness of Carbon and Boron Nitride Polymorphs from First Principles Calculations. *Physical Review B* **2006**, *73* (6), 1–7. <https://doi.org/10.1103/PhysRevB.73.064304>.
- (45) Jungwirth, N. R.; Fuchs, G. D. Optical Absorption and Emission Mechanisms of Single Defects in Hexagonal Boron Nitride. *Physical Review Letters* **2017**, *119* (5), 1–6. <https://doi.org/10.1103/PhysRevLett.119.057401>.
- (46) Chew, H. Dielectric Particles. *Physical Review A* **1988**, *38* (7), 3410–3416.
- (47) Schniepp, H.; Sandoghdar, V. Spontaneous Emission of Europium Ions Embedded in Dielectric Nanospheres. *Physical Review Letters* **2002**, *89* (25), 1–4. <https://doi.org/10.1103/PhysRevLett.89.257403>.
- (48) Inam, F. A.; Grogan, M. D. W.; Rollings, M.; Gaebel, T.; Say, J. M.; Bradac, C.; Birks, T. A.; Wadsworth, W. J.; Castelletto, S.; Rabeau, J. R.; Steel, M. J. Emission and Nonradiative Decay of Nanodiamond NV Centers in a Low Refractive Index Environment. *ACS Nano* **2013**, *7* (5), 3833–3843. <https://doi.org/10.1021/nn304202g>.
- (49) Chejanovsky, N.; Kim, Y.; Zappe, A.; Stuhlhofer, B.; Taniguchi, T.; Watanabe, K.; Dasari, D.; Finkler, A.; Smet, J. H.; Wrachtrup, J. Quantum Light in Curved Low Dimensional Hexagonal Boron Nitride Systems. *Scientific Reports* **2017**, *7* (1), 1–14. <https://doi.org/10.1038/s41598-017-15398-2>.
- (50) Ikuno, T.; Sainsbury, T.; Okawa, D.; Fréchet, J. M. J.; Zettl, A. Amine-Functionalized Boron Nitride Nanotubes. *Solid State Communications* **2007**, *142* (11), 643–646. <https://doi.org/10.1016/j.ssc.2007.04.010>.

- (51) Sainsbury, T.; Ikuno, T.; Okawa, D.; Pacilé, D.; Fréchet, J. M. J.; Zettl, A. Self-Assembly of Gold Nanoparticles at the Surface of Amine- and Thiol-Functionalized Boron Nitride Nanotubes. *The Journal of Physical Chemistry C* **2007**, *111* (35), 12992–12999. <https://doi.org/10.1021/jp072958n>.
- (52) Aharonovich, I.; Englund, D.; Toth, M. Solid-State Single-Photon Emitters. *Nature Photonics* **2016**, *10* (10), 631–641. <https://doi.org/10.1038/nphoton.2016.186>.
- (53) Rudolph, T. Why I Am Optimistic about the Silicon-Photonic Route to Quantum Computing. *APL Photonics* **2016**, *2* (030901), 1–19. <https://doi.org/10.1063/1.4976737>.
- (54) Schlüssel, Y.; Lenz, T.; Rohner, D.; Bar-Haim, Y.; Bougas, L.; Groswasser, D.; Kieschnick, M.; Rozenberg, E.; Thiel, L.; Waxman, A.; Meijer, J.; Maletinsky, P.; Budker, D.; Folman, R. Widefield Imaging of Superconductor Vortices with Electron Spins in Diamond. *Physical Review Applied* **2018**, *10* (034032), 1–6. <https://doi.org/10.1103/PhysRevApplied.10.034032>.
- (55) Toyli, D.; Christle, D.; Alkauskas, A.; Buckley, B.; Van de Walle, C.; Awschalom, D. Measurement and Control of Single Nitrogen-Vacancy Center Spins above 600 K. *Physical Review X* **2012**, *2* (3), 1–7. <https://doi.org/10.1103/PhysRevX.2.031001>.
- (56) Schröder, T.; Gädeke, F.; Banholzer, M. J.; Benson, O. Ultrabright and Efficient Single-Photon Generation Based on Nitrogen-Vacancy Centres in Nanodiamonds on a Solid Immersion Lens. *New Journal of Physics* **2011**, *13* (055017), 1–9. <https://doi.org/10.1088/1367-2630/13/5/055017>.
- (57) He, Y. M.; He, Y.; Wei, Y. J.; Wu, D.; Atatüre, M.; Schneider, C.; Höfling, S.; Kamp, M.; Lu, C. Y.; Pan, J. W. On-Demand Semiconductor Single-Photon Source with near-Unity Indistinguishability. *Nature Nanotechnology* **2013**, *8* (3), 213–217. <https://doi.org/10.1038/nnano.2012.262>.
- (58) Neu, E.; Steinmetz, D.; Riedrich-Möller, J.; Gsell, S.; Fischer, M.; Schreck, M.; Becher, C. Single Photon Emission from Silicon-Vacancy Colour Centres in Chemical Vapour Deposition Nano-Diamonds on Iridium. *New Journal of Physics* **2011**, *13* (025012), 1–21. <https://doi.org/10.1088/1367-2630/13/2/025012>.
- (59) Hausmann, B. J. M.; Shields, B. J.; Quan, Q.; Chu, Y.; De Leon, N. P.; Evans, R.; Burek, M. J.; Zibrov, A. S.; Markham, M.; Twitchen, D. J.; Park, H.; Lukin, M. D.; Lončar, M. Coupling of NV Centers to Photonic Crystal Nanobeams in Diamond. *Nano Letters* **2013**, *13* (12), 5791–5796. <https://doi.org/10.1021/nl402174g>.

- (60) Schmidgall, E.; Chakravarthi, S.; Gould, M.; Christen, I.; Hestroffer, K.; Hatami, F.; Fu, K.-M. Frequency Control of Single Quantum Emitters in Integrated Photonic Circuits. *Nano Letters* **2018**, *18*, 1175–1179. <https://doi.org/10.1021/acs.nanolett.7b04717>.
- (61) Jungwirth, N. R.; Calderon, B.; Ji, Y.; Spencer, M. G.; Flatté, M. E.; Fuchs, G. D. Temperature Dependence of Wavelength Selectable Zero-Phonon Emission from Single Defects in Hexagonal Boron Nitride. *Nano Letters* **2016**, *16* (10), 6052–6057. <https://doi.org/10.1021/acs.nanolett.6b01987>.
- (62) Grosso, G.; Moon, H.; Lienhard, B.; Ali, S.; Efetov, D. K.; Furchi, M. M.; Jarillo-Herrero, P.; Ford, M. J.; Aharonovich, I.; Englund, D. Tunable and High Purity Room-Temperature Single Photon Emission from Atomic Defects in Hexagonal Boron Nitride. *Nature Communications* **2016**, *8* (705), 1–8. https://doi.org/10.1364/CLEO_AT.2017.JM3E.5.
- (63) Proscia, N. V.; Shotan, Z.; Jayakumar, H.; Reddy, P.; Dollar, M.; Alkauskas, A.; Doherty, M.; Meriles, C. A.; Menon, V. M. Near-Deterministic Activation of Room Temperature Quantum Emitters in Hexagonal Boron Nitride. *Optica* **2017**, *5* (9), 1128–1134. <https://doi.org/10.1364/OPTICA.5.001128>.
- (64) Falin, A.; Cai, Q.; Santos, E. J. G.; Scullion, D.; Qian, D.; Zhang, R.; Yang, Z.; Huang, S.; Watanabe, K.; Taniguchi, T.; Barnett, M. R.; Chen, Y.; Ruoff, R. S.; Li, L. H. Mechanical Properties of Atomically Thin Boron Nitride and the Role of Interlayer Interactions. *Nature Communications* **2017**, *8*, 1–9. <https://doi.org/10.1038/ncomms15815>.
- (65) Li, X.; Shepard, G. D.; Cupo, A.; Camporeale, N.; Shayan, K.; Luo, Y.; Meunier, V.; Strauf, S. Nonmagnetic Quantum Emitters in Boron Nitride with Ultranarrow and Sideband-Free Emission Spectra. *ACS Nano* **2017**, *11* (7), 6652–6660. <https://doi.org/10.1021/acsnano.7b00638>.
- (66) Kuno, M.; Fromm, D. P.; Gallagher, A.; Nesbitt, D. J.; Micic, O. I.; Nozik, A. J. Fluorescence Intermittency in Single InP Quantum Dots. *Nano Letters* **2001**, *1* (10), 557–564. <https://doi.org/10.1021/nl010049i>.
- (67) Kuno, M.; Fromm, D. P.; Hamann, H. F.; Gallagher, A.; Nesbitt, D. J. “On”/“off” Fluorescence Intermittency of Single Semiconductor Quantum Dots. *The Journal of Chemical Physics* **2001**, *115*, 1028–1040. <https://doi.org/10.1063/1.1377883>.
- (68) Shimizu, K. T.; Neuhauser, R. G.; Leatherdale, C. A.; Empedocles, S. A.; Woo, W. K.; Bawendi, M. G. Blinking Statistics in Single Semiconductor Nanocrystal Quantum Dots. *Physical Review B* **2001**, *63* (205316), 1–5. <https://doi.org/10.1103/PhysRevB.63.205316>.

- (69) Frantsuzov, P.; Kuno, M.; Jankó, B.; Marcus, R. A. Universal Emission Intermittency in Quantum Dots, Nanorods and Nanowires. *Nature Physics* **2008**, *4* (7), 519–522. <https://doi.org/10.1038/nphys1001>.
- (70) Bharadwaj, P.; Novotny, L. Robustness of Quantum Dot Power-Law Blinking. *Nano Letters* **2011**, *11* (5), 2137–2141. <https://doi.org/10.1021/nl200782v>.
- (71) Bradac, C.; Gaebel, T.; Naidoo, N.; Sellars, M. J.; Twamley, J.; Brown, L. J.; Barnard, A. S.; Plakhotnik, T.; Zvyagin, A. V; Rabeau, J. R. Observation and Control of Blinking Nitrogen-Vacancy Centres in Discrete Nanodiamonds. *Nature Nanotechnology* **2010**, *5* (5), 345–349.
- (72) Berhane, A. M.; Bradac, C.; Aharonovich, I. Photoinduced Blinking in a Solid-State Quantum System. *Physical Review B* **2017**, *96* (4). <https://doi.org/10.1103/PhysRevB.96.041203>.
- (73) Castelletto, S.; Johnson, B. C.; Ivády, V.; Stavrias, N.; Umeda, T.; Gali, A.; Ohshima, T. A Silicon Carbide Room-Temperature Single-Photon Source. *Nature Materials* **2014**, *13* (2), 151–156. <https://doi.org/10.1038/nmat3806>.
- (74) Yuan, G.; Gómez, D. E.; Kirkwood, N.; Boldt, K.; Mulvaney, P. Two Mechanisms Determine Quantum Dot Blinking. *ACS Nano* **2018**, *12* (4), 3397–3405. <https://doi.org/10.1021/acsnano.7b09052>.
- (75) Efros, A.I.; Rosen, M. Random Telegraph Signal in the Photoluminescence Intensity of a Single Quantum Dot. *Physical Review Letters* **1997**, *78* (6), 1110–1113. <https://doi.org/10.1103/PhysRevLett.78.1110>.
- (76) Stefani, F. D.; Hoogenboom, J. P.; Barkai, E. Beyond Quantum Jumps: Blinking Nanoscale Light Emitters. *Physics Today* **2009**, *62* (2), 34–39. <https://doi.org/10.1063/1.3086100>.
- (77) Li, W.; Liang, L.; Zhao, S.; Zhang, S.; Xue, J. Fabrication of Nanopores in a Graphene Sheet with Heavy Ions: A Molecular Dynamics Study. *Journal of Applied Physics* **2013**, *114* (234304), 1–6. <https://doi.org/10.1063/1.4837657>.
- (78) Bai, Z.; Zhang, L.; Li, H.; Liu, L. Nanopore Creation in Graphene by Ion Beam Irradiation: Geometry, Quality, and Efficiency. *ACS Applied Materials and Interfaces* **2016**, *8* (37), 24803–24809. <https://doi.org/10.1021/acsmi.6b06220>.

- (79) Elbadawi, C.; Tran, T. T.; Kolíbal, M.; Šíkola, T.; Scott, J.; Cai, Q.; Li, L. H.; Taniguchi, T.; Watanabe, K.; Toth, M.; Aharonovich, I.; Lobo, C.; Lin, Y.; Connell, J. W.; Watanabe, K.; Taniguchi, T.; Kanda, H.; Caldwell, J. D.; Kretinin, A. V.; Chen, Y.; Giannini, V.; Fogler, M. M.; Francescato, Y.; Ellis, C. T.; Tischler, J. G.; Woods, C. R.; Giles, A. J.; Uosaki, K.; Elumalai, G.; Noguchi, H.; Masuda, T.; Lyalin, A.; Nakayama, A.; Taketsugu, T.; Tran, T. T.; Bray, K.; Ford, M. J.; Toth, M.; Aharonovich, I.; Dai, S.; Fei, Z.; Ma, Q.; Rodin, A.; Wagner, M.; McLeod, A.; Liu, M.; Gannett, W.; Regan, W.; Watanabe, K.; Wang, L.; Wu, B.; Jiang, L.; Chen, J.; Li, Y.; Guo, W.; Hu, P.; Liu, Y.; Sharma, S.; Kalita, G.; Vishwakarma, R.; Zulkifli, Z.; Tanemura, M.; Liao, Y.; Tu, K.; Han, X.; Hu, L.; Connell, J. W.; Chen, Z.; Lin, Y.; Liu, Z.; Ma, L.; Shi, G.; Zhou, W.; Gong, Y.; Lei, S.; Yang, X.; Zhang, J.; Yu, J.; Hackenberg, K. P.; Babakhani, A.; Idrobo, J.-C.; Vajtai, R.; Lou, J.; Ajayan, P. M.; Meyer, J. C.; Chuvilin, A.; Algara-Siller, G.; Biskupek, J.; Kaiser, U.; Sun, L.; Banhart, F.; Warner, J.; Ryu, G. H.; Park, H. J.; Ryou, J.; Park, J.; Lee, J.; Kim, G.; Shin, H. S.; Bielawski, C. W.; Ruoff, R. S.; Hong, S.; Lee, Z.; Linas, S.; Fulcrand, R.; Cauwet, F.; Poinso, B.; Brioude, A.; Martin, A. A.; Bahm, A.; Bishop, J.; Aharonovich, I.; Toth, M.; Taniguchi, T.; Watanabe, K.; Toth, M.; Arumainayagam, C. R.; Lee, H.-L.; Nelson, R. B.; Haines, D. R.; Gunawardane, R. P.; Utke, I.; Hoffmann, P.; Melngailis, J.; Randolph, S. J.; Fowlkes, J. D.; Rack, P. D.; Utke, I.; Goelzhaeuser, A.; Toth, M.; Lobo, C. J.; Knowles, W. R.; Phillips, M. R.; Postek, M. T.; Vladar, A. E.; Martin, A. A.; Phillips, M. R.; Toth, M.; Martin, A. A.; McCredie, G.; Toth, M.; Joy, D.; Luo, S.; Hovington, P.; Drouin, D.; Gauvin, R. Electron Beam Directed Etching of Hexagonal Boron Nitride. *Nanoscale* **2016**, *8* (36), 16182–16186. <https://doi.org/10.1039/C6NR04959A>.
- (80) Buchheim, J.; Wyss, R. M.; Shorubalko, I.; Park, H. G. Understanding the Interaction between Energetic Ions and Freestanding Graphene towards Practical 2D Perforation. *Nanoscale* **2016**, *8* (15), 8345–8354. <https://doi.org/10.1039/C6NR00154H>.
- (81) Fox, D. S.; Zhou, Y.; Maguire, P.; O'Neill, A.; Ócoileáin, C.; Gatensby, R.; Glushenkov, A. M.; Tao, T.; Duesberg, G. S.; Shvets, I. V.; Abid, M.; Abid, M.; Wu, H. C.; Chen, Y.; Coleman, J. N.; Donegan, J. F.; Zhang, H. Nanopatterning and Electrical Tuning of MoS₂ Layers with a Subnanometer Helium Ion Beam. *Nano Letters* **2015**, *15* (8), 5307–5313. <https://doi.org/10.1021/acs.nanolett.5b01673>.
- (82) Park, H.; Shin, G. H.; Lee, K. J.; Choi, S. Atomic-Scale Etching of Hexagonal Boron Nitride for Device Integration Based on Two-Dimensional Materials. *Nanoscale* **2018**, *10*, 15204–15212. <https://doi.org/10.1039/c8nr02451k>.
- (83) Abdi, M.; Chou, J.-P.; Gali, A.; Plenio, M. B. Color Centers in Hexagonal Boron Nitride Monolayers: A Group Theory and Ab Initio Analysis. *ACS Photonics* **2017**, *5*, 1967–1976. <https://doi.org/10.1021/acsphotonics.7b01442>.

- (84) Wiktor, J.; Pasquarello, A. Absolute Deformation Potentials of Two-Dimensional Materials. *Physical Review B* **2016**, *94* (24), 1–8. <https://doi.org/10.1103/PhysRevB.94.245411>.
- (85) Lopez-Bezanilla, A.; Huang, J.; Terrones, H.; Sumpter, B. G. Boron Nitride Nanoribbons Become Metallic. *Nano Letters* **2011**, *11* (8), 3267–3273. <https://doi.org/10.1021/nl201616h>.
- (86) Zeng, H.; Zhi, C.; Zhang, Z.; Wei, X.; Wang, X.; Guo, W.; Bando, Y.; Golberg, D. “White Graphenes”: Boron Nitride Nanoribbons via Boron Nitride Nanotube Unwrapping. *Nano Letters* **2010**, *10* (12), 5049–5055. <https://doi.org/10.1021/nl103251m>.
- (87) Girit, Ç. Ö.; Meyer, J. C.; Erni, R.; Rossell, M. D.; Kisielowski, C.; Yang, L.; Park, C.; Crommie, M. F.; Cohen, M. L.; Louie, S. G.; Zettl, A. Graphene at the Edge : Stability and Dynamics. *Science (New York, N.Y.)* **2009**, *323* (5922), 1705–1708. <https://doi.org/10.1126/science.1166999>.
- (88) Cheng, Y. C.; Wang, H. T.; Zhu, Z. Y.; Zhu, Y. H.; Han, Y.; Zhang, X. X.; Schwingenschlögl, U. Strain-Activated Edge Reconstruction of Graphene Nanoribbons. *Physical Review B* **2012**, *85* (7), 1–5. <https://doi.org/10.1103/PhysRevB.85.073406>.
- (89) Noh, G.; Choi, D.; Kim, J.-H.; Im, D.-G.; Kim, Y.-H.; Seo, H.; Lee, J. Stark Tuning of Single-Photon Emitters in Hexagonal Boron Nitride. *Nano Letters* **2018**, *acs.nanolett.8b01030*. <https://doi.org/10.1021/acs.nanolett.8b01030>.
- (90) Suk, J. W.; Kitt, A.; Magnuson, C. W.; Hao, Y.; Ahmed, S.; An, J.; Swan, A. K.; Goldberg, B. B.; Ruoff, R. S. Transfer of CVD-Grown Monolayer Graphene onto Arbitrary Substrates. *ACS Nano* **2011**, *5* (9), 6916–6924. <https://doi.org/10.1021/nn201207c>.
- (91) Newman, M. E. J. Power Laws, Pareto Distributions and Zipf’s Law. *Contemporary Physics* **2005**, *46* (5), 323–351. <https://doi.org/10.1080/00107510500052444>.
- (92) Frantsuzov, P. A.; Volkan-Kacso, S.; Janko, B. Model of Fluorescence Intermittency of Single Colloidal Semiconductor Quantum Dots Using Multiple Recombination Centers. *Physical Review Letters* **2009**, *103* (20). <https://doi.org/10.1103/PhysRevLett.103.207402>.
- (93) Crouch, C. H.; Sauter, O.; Wu, X.; Purcell, R.; Querner, C.; Drndic, M.; Pelton, M. Facts and Artifacts in the Blinking Statistics of Semiconductor Nanocrystals. *Nano Letters* **2010**, *10* (5), 1692–1698. <https://doi.org/10.1021/nl100030e>.

- (94) Schmidt, R.; Krasselt, C.; Göhler, C.; von Borczyskowski, C. The Fluorescence Intermittency for Quantum Dots Is Not Power-Law Distributed: A Luminescence Intensity Resolved Approach. *ACS Nano* **2014**, 8 (4), 3506–3521. <https://doi.org/10.1021/nn406562a>.
- (95) Hu, F.; Cao, Z.; Zhang, C.; Wang, X.; Xiao, M. Defect-Induced Photoluminescence Blinking of Single Epitaxial InGaAs Quantum Dots. *Scientific Reports* **2015**, 5, 8898. <https://doi.org/10.1038/srep08898>.
- (96) Noh, G.; Choi, D.; Kim, J.-H.; Im, D.-G.; Kim, Y.-H.; Seo, H.; Lee, J. Stark Tuning of Single-Photon Emitters in Hexagonal Boron Nitride. *Nano Lett.* **2018**, 18, 4710.
- (97) Dietrich, A.; Doherty, M. W.; Aharonovich, I.; Kubanek, A. Solid-State Single Photon Source with Fourier Transform Limited Lines at Room Temperature. *Phys. Rev. B* **2020**, 101 (8), 081401. <https://doi.org/10.1103/PhysRevB.101.081401>.